Tracing future spring and summer drying in southern Africa to tropical lows and the Congo Air Boundary

Article

Accepted Version

Tracing future spring and summer drying in southern Africa to tropical lows and the Congo Air Boundary

Emma Howard* and Richard Washington

School of Geography and the Environment, University of Oxford, Oxford, United Kingdom

**Corresponding author address:* Emma Howard, South Parks Road, Oxford OX13QY United Kingdom

E-mail: emma.howard@reading.ac.uk

ABSTRACT

In southern Africa, models from the 5th Coupled Model Intercomparison Project (CMIP5) predict robust future drying associated with a delayed rainy season onset in the Austral spring and a range of wetting and drying patterns in the Austral summer. This paper relates these rainfall changes to dynamical shifts in two classes of weather systems: the Congo Air Boundary (CAB) and tropical lows. Objective algorithms are used to track these features in CMIP5 model output. It is then established that the climatological locations and frequencies of these systems are reasonably well represented in the CMIP5 models. RCP8.5 end of 21st century projections are compared with historical end of 20th century simulations. Future projections in tropical low locations and frequencies diverge, but indicate an overall average decrease of 15% and in some cases a northward shift. The projected spatial change in the tropical low frequency distribution is weakly positively correlated to the projected spatial change in the Austral summer rainfall distribution. Meanwhile, future projections indicate a 13% increase in CAB frequency from October to December. This is associated with the gradual climatological CAB breakdown occurring half a month later on average in end of 21st century RCP8.5 projections. A delay in the gradual seasonal decline of the CAB prevents rainfall to the south of the CAB's mean position, most of which is shown to occur on CAB breakdown days, hence creating the Austral spring drying signal and delayed wet season onset. Inter-model variability in the magnitude of CAB frequency increase is able to explain inter-model variability in the projected drying.

1. Introduction

CMIP5 based rainfall projections exhibit a rainfall decline over southern Africa which is strongest in the October, November and December (OND) season (James and Washington, 2013). This rainfall decline has been linked with a delay in the onset date of the rainy season (Dunning et al., 2018), and in many models comes with an increase in rainfall in central Africa in the same season (Aloysius et al., 2016; Creese et al., 2019). Southern Africa is highly vulnerable to climate related socio-economic risk, as the regional water resource supports the local food-energy-water nexus (Conway et al., 2015). In particular, rainy season onset and cessation dates are particularly important for farmers and other stakeholders (Hachigonta et al., 2008). Some studies have found consistent delays of southern African wet season onset in satellite and gauge-based observational datasets covering the late 20^{th} and early 21^{st} centuries (e.g., Jiang et al., 2019; Kniveton et al., 2009). Delayed rainfall onset would shorten the growing season, as no corresponding delay in cessation has been projected (Dunning et al., 2018). This will reduce the agricultural viability of the region and have follow-on effects on regional food security and economic growth (Lobell et al., 2008; Schlenker and Lobell, 2010).

At first glance, the southern African drying trend appears to follow that of the broader subtropical drying trend. However, closer analysis reveals that in southern Africa, the drying occurs primarily north of the subtropical rainfall minimum (Scheff and Frierson, 2012a,b). Furthermore, while the subtropical drying signal is largely characterized by an increase in the magnitude of the difference between precipitation and evaporation (P-E), in southern Africa evaporation decreases in line with precipitation, so that P-E does not change considerably. Lazenby et al. (2018) demonstrated that the southern African drying trend is primarily a consequence of circulation changes, rather than thermodynamic mechanisms such as dry-get-drier (Held and Soden, 2006) or upped-ante (Chou

et al., 2009). Thus, the southern African drying trend is dynamically unique and requires a bespoke approach.

Some work has been done on understanding the dynamics of projected rainfall change in southern Africa. Lazenby et al. (2018) found that this change could be viewed as a northward shift of the African rain-band, while Dunning et al. (2018) linked the delayed onset of OND rains in southern Africa to relative changes in the strengths of the Saharan and Angolan heat lows. Munday and Washington (2019) found a complementary result: models with a deeper future climatological Angola heat low showed a higher intensity of drying. Similarly, Cook and Vizy (2013) observed a strengthening of the Angola low in regional climate model simulations. However, little work has been done to directly link rainfall change to changes in precipitating weather systems.

Meanwhile, less work has looked at rainfall change in December - February (DJF), the peak of the wet season (Van Heerden and Taljaard, 1998). Model projections disagree in this season, although Lazenby et al. (2018) suggest that inter-model differences in SST trends in adjacent oceans may explain the diverse range of model projections. Once again, the characteristics of the future change patterns of atmospheric features on synoptic timescales has not been studied.

Since atmospheric circulation on climatological timescales is the aggregation of synoptic weather systems, future circulation change hinges on the response of synoptic weather systems to a warmer atmosphere. However, the synoptic weather systems that occur in the southern African tropical margins are under-studied. The representation of such synoptic weather systems in CMIP5 models and their future change has not been studied. This knowledge gap ensures that the synoptic context of the future change signal in this region, and whether or not a specific class of weather system may deliver the projected change, is unknown.

This paper focusses on two local classes of weather systems which occur in the latitudinal band of the advancing spring rains and have previously been associated with rainfall variability. The first

is the Congo Air Boundary (CAB), a combined surface dryline and convergence line that marks the boundary between tropical and subtropical weather zones in the Austral spring (Howard and Washington, 2019). The second class of weather systems considered are tropical lows, cyclonic rotating vortices that form in the Austral summer and tend to cluster near 20°S, creating the climatological Angola tropical low (Howard and Washington, 2018). By examining the representation of the CAB and tropical lows in historical coupled climate models, this work follows a process based model evaluation framework. After establishing whether these systems are well modelled, we then proceed to studying process based projections. This involves investigating how the CAB and tropical lows are projected to change according to RCP8.5 end of 21st century simulations.

Both of these weather systems were identified by Taljaard (1986) as two of the ten most important factors that influence the weather over southern Africa. Crucially, they both operate on length-scales that are large enough to be resolved in CMIP5 models. The focus of this work is on the Austral spring and summer seasons, since the former is the season with the strongest rainfall change, and the latter is the main rainy season. Our analysis will show that changes in tropical lows and the CAB are vitally important for future projections of southern African precipitation, as they directly influence the delivery of model precipitation. However, this result does not preclude changes in other factors, including the distribution of sea surface temperatures, the subtropical jet and high-pressure belt, and upper-level waves, from also playing a role. Indeed, it is possible that the circulation changes of tropical lows and the CAB are linked to changes in these other systems.

The CAB has historically been defined as the confluence zone between the Congo Airmass, a moist and convectively active region of air that sits over the Congo rainforest, and the drier trade easterlies that cross southern Africa and originate from the Indian Ocean (Taljaard, 1972). The CAB was originally discussed in the context of identifying the elusive ITCZ over southern and eastern Africa (Taljaard, 1953). It was argued that the CAB could not be the ITCZ itself, as both

airmasses involved originate from the Southern Hemisphere (the Congo Airmass being associated with the recurvature of the south Atlantic trade winds, known locally as the low level westerlies, e.g., Leroux (2001)). However, the importance of the CAB for southern African rainfall was undisputed (Torrance, 1979).

Despite its importance to the local climate, no systematic study of the representation of the CAB in reanalysis or model products had been performed before Howard and Washington (2019). They optimized an edge-detecting algorithm and a ridge-detecting algorithm to pick out sharp gradients in specific humidity and ridges in wind convergence that were associated with the southern portion of the CAB. They distinguished between the 'dryline' CAB and a 'convergence line' CAB based on the choice of algorithm and determined that although the two were closely comparable, the 'dryline' algorithm was slightly more reliable. Howard and Washington (2019) also identified the Kalahari Discontinuity (KD), a similar near-surface dryline/convergence line system located further south and oriented parallel to the west coast of southern Africa, that forms after the CAB breaks down in October and November. They confirmed that the CAB latitude and detection frequency were closely linked to the interannual variability of spring rainfall over southern Africa. This suggests that the future change of the CAB has potential explanatory power for the OND drying.

Southern African tropical lows are synoptic-scale cyclonic vortices with depths up to 500 hPa that track predominantly westward across the southern African continent (Howard and Washington, 2018). They are precipitating systems, and cluster in eastern Angola and western Zambia, where they tend to become semi-stationary (Howard et al., 2019). In southern Africa, tropical lows have been most commonly studied in the form of their climatological mean, the Angola tropical low (e.g., Cook et al., 2004; Crétat et al., 2018; Pascale et al., 2019). Since the Angola tropical low has been closely linked to interannual rainfall variability (Reason and Jagadheesha,

2005; Cook et al., 2004), considerable attention has been paid to how it is simulated in various models. Lazenby et al. (2016) and Munday and Washington (2017) both found that the Angola low is excessively strong in historical climate models, and linked this to the wet bias over southern Africa. However, the representation of the Angola tropical low on synoptic timescales in CMIP5 models, and its future change, has not yet been assessed.

The goal of this paper is to express projected rainfall changes from the viewpoint of projected changes in synoptic weather systems. This involves first linking the spring drying signal to projected changes in characteristics of the CAB, and also linking the summer inter-model spread of rainfall projections with the inter-model spread of changes to the spatial distribution and frequencies of tropical lows and the CAB. To achieve this aim, the paper proceeds as follows. In section 2, the models, datasets and feature identification algorithms are described. In section 3, we consider the historical representation of the CAB, the CAB's projected future change and the rainfall implications of that projected change. In section 4, we perform a similar analysis on tropical lows. In the final section, we summarize the importance of this work for understanding rainfall change in southern Africa.

2. Methods

a. Models and Reanalysis Datasets

A selection of 25 CMIP5 models has been used in this study, based on the availability of the appropriate model output variables. To study the CAB, we require daily surface level specific humidity and temperature data, which 18 of these models had available. To study tropical lows, we required 6 hourly wind data on pressure levels, which was available in a different subset of 18 models. The model names, creators and grid-spacings are shown in table 1, together with a list of

which models were used to study the CAB and tropical lows. For each model, 30 years of end of 20th century coupled climate model output were examined, and compared to 30 years of end of 21st century model output generated under the RCP8.5 coupled model scenario. More precisely, the CAB was studied between August '70 and December '99 of each century, while tropical lows were studied between November '69 and March '99. The simulated historical climatology of each feature was compared to the reanalysis climatologies from three reanalysis products: ERA-5, ERA-Interim and MERRA-2. Reanalysis climatologies were taken from the 30-year period 1980-2010.

The CAB has been identified between August and December, and its correlation with rainfall change has been studied between October and December. The former season has been chosen because this is the season in which the CAB is present in southern Africa, and the season in which validation against the results of Howard and Washington (2019) was possible. The latter season was chosen because it is the season of maximum rainfall decline in southern Africa (Munday and Washington, 2019). Tropical lows were identified between November and March, and their influence on future rainfall change was studied between December and February. Again, the former is the season in which tropical lows are present in southern Africa (Howard et al., 2019). The latter is the main wet season in southern Africa, and is also the season in which the contribution of tropical lows towards southern African rainfall is most significant (Howard et al., 2019). The OND precipitation decline across the two 30-year time periods is greater than the 30-year decadal standard deviation as calculated from the corresponding pre-industrial control experiments in over 50% of the models considered, as indicated by Supplementary Figure S1. This was not the case in DJF.

b. Congo Air Boundary

This paper adapts the methodology of Howard and Washington (2019) to identify the CAB in CMIP5 models. Because they studied the CAB in a high resolution ($\sim 0.25°$) reanalysis dataset, and the models employed here have resolutions ranging from $\sim 1°$ - $3°$, this methodology needs a few modifications in order to transfer over to lower resolutions. Properties of the CAB are dependent on the resolution of the input data, and so all models and reanalyses are regridded to a $2° \times 2°$ grid.

While Howard and Washington (2019) used both wind convergence and humidity to detect the CAB, the present study only uses humidity, and focusses solely on what Howard and Washington (2019) refer to as the 'dryline CAB'. This choice was made because Howard and Washington (2019) found that the dryline CAB was more reliable and easily detected than the convergence line CAB. Near-surface relative humidity gradients, rather than specific humidity gradients, have been used to calculate the CAB location. This choice has been made to allow for easier comparison between historical and RCP8.5 experiments, given that near-surface specific humidity generally increases by a factor of about two across the tropics by the end of the 21st century in the RCP8.5 scenario.

The algorithm used to detect the CAB is as follows. Figure 1 shows the algorithm applied to a sample day (9/9/1999) from a sample model (ACCESS1.3).

1. The 2m relative humidity is calculated from 2m daily mean air temperature (tas), 2m daily mean specific humidity (huss) and surface pressure (sp), where these fields are available. Where they are not available, the 1000 hPa pressure level relative humidity (hur) is used instead.

2. Relative humidity is interpolated to a $2^\circ \times 2^\circ$ grid using a nearest neighbor interpolation scheme. This scheme is chosen in order to avoid differentially smoothing humidity gradients in the higher resolution datasets during the regridding process. The left panel of Figure 1 shows the regridded field.

3. In keeping with the Canny (Canny, 1986) algorithm, a Gaussian filter with a 2° radius is used to smooth the relative humidity field. The magnitude (M) and direction (θ) of the gradient were then calculated using finite differences.

4. Canny edges were calculated as per Howard and Washington (2019), thresholding the magnitude of the humidity gradient such that it must undergo an absolute change of $\Delta RH = 40\%$ between grid cells across a Canny edge in order for a grid cell to qualify as a CAB. The center panel of Figure 1 shows the Canny edges identified on the sample model day, colored by the orientation angle of the edge.

5. Canny edges were filtered to retain instances with $-\frac{\pi}{4} < \theta < \frac{\pi}{6}$ and restricted to latitudes between 5° - 18°S.

6. At least 3 qualifying dryline grid cells were required to be detected at the same time in order for a CAB to be registered. The resultant CAB grid-cells shown in the right panel of Figure 1 on the sample model day.

The KD is also extracted from the calculated set of Canny edges. It is restricted to latitudes below 12°S and angles between $\frac{\pi}{6} < \theta < \frac{\pi}{2}$, consistent with Howard and Washington (2019). No minimum grid cell thresholds are applied in this case. As described above, three reanalysis products, ERA-5, ERA-Interim and MERRA2, have been included in this study. The thresholds described above were manually optimized so that the seasonal cycle of the relative humidity based

CAB in the coarsened ERA-5 using the methodology of this paper was qualitatively similar to the high resolution specific humidity ERA-5 results of Howard and Washington (2019).

Figure 2 shows the near-surface relative humidity and identified CAB points for the same case study day in early September in historical models and reanalyses. The atmospheric states on this chosen day will be in different synoptic setups. Nevertheless, a well-defined CAB is identified on this day in all of the CMIP5 models.

With the daily CAB positions calculated, climatologies of properties such as latitude, frequencies and extent can be computed and compared. Here, the extent is calculated by counting the total number of CAB grid cells on a given day. This gives an approximate measure of the lateral extent of the CAB.

c. Tropical lows

The methodology used to identify tropical low events follows Howard et al. (2019). We apply the TRACK algorithm (Hodges, 1994, 1999). The application of TRACK to CMIP5 model experiments has previously been documented by Rastogi et al. (2018) and Bengtsson et al. (2007). Howard et al. (2019) identified southern African tropical lows using 6-hourly vertical mean vorticity averaged across pressure levels at 600, 700 and 800 hPa. However, 6-hourly CMIP5 pressure level model data was only available at 850 and 500 hPa, and so these model levels have been used instead. A comparison between the results of using this set-up and using 600, 700 and 800 hPa daily vorticity was considered for a subset of 9 models and no significant difference was found (not shown).

The data preparation algorithm was as follows. At each vertical level and for each 6-hourly time-step, vertical vorticity was calculated from the zonal and meridional wind components at a T63 resolution, using the python package windspharm. The vertical average was taken, and then

a Sardeshmukh and Hoskins (1988) filter was applied to smooth the spectral cut-off. Cyclonic vorticity extrema with $\zeta < -5 \times 10^{-6} s^{-1}$ were then identified and linked using the TRACK algorithm, as detailed in Howard et al. (2019) and Hodges et al. (2017). Once these vortex tracks were identified, they were filtered for southern African tropical lows using the following criteria:

1. Tracks must spend at least one time step over land;
2. Track longevity must be at least one day;
3. The filtered vertical mean relative vorticity must satisfy $\zeta < -3 \times 10^{-5} s^{-1}$ in at least one 6-hourly time-step;
4. There must be coincident cyclonic vorticity at 500, 850 hPa for a continuous 24 hour period;
5. The genesis location must not be in the Atlantic; and
6. The genesis location must be north of 25° S.

Justification for these criteria are given in Howard et al. (2019): briefly, they exclude extra-tropical cyclones, coastally trapped Kelvin waves, heat lows, and spurious weak events. A sample track longitude Hovmöller plot for each of the models and the reanalysis over one historical year is shown in Figure 3. The models reveal a mixture of track behaviours.

Following the identification of tropical lows, rainfall is attributed to tropical lows by making the assumption that all daily rainfall that fell within a 5° radius of a tropical low centroid was attributable to that tropical low. This radius was shown to be appropriate for southern African tropical lows by Howard et al. (2019) and is consistent with many previous studies of tropical lows and tropical cyclones (Baray et al., 2003; Dare et al., 2012; Khouakhi et al., 2017; Lavender and Abbs, 2013).

3. The Congo Air Boundary

a. Representation in Historical Climate Models

The aim of this section is to determine whether or not the CAB is well represented in the CMIP5 historical simulations under consideration for the period from 1970-2000. Figures are designed to be comparable with the ERA-5 based study of the CAB presented in Howard and Washington (2019), and modelled CAB properties are compared with the coarsened ERA-5 reanalysis. The KD is also briefly considered.

Figure 4 indicates the climatological location of the CAB and KD in each climate model and reanalysis product, based on the frequency the CAB is detected at each interpolated $2° \times 2°$ grid-box. It is evident that the CAB is detected with similar frequencies and locations in most of the models as in the reanalysis products. There is a range of variation across the models, however. CMRM-CM5, GFDL-CM3 and the ACCESS models show concentrated, high intensity CAB locations with a diagonal orientation from west of Lake Victoria through to south west Angola. NorESM1-M and bcc-csm1-1m show heat-maps with a distinct north and south peak. All three IPSL models show low CAB detection frequencies in the east. This is particularly interesting since the IPSL-CM5A models have previously been shown to be outliers in East Africa, lacking the moisture-rainfall relationship present in most other models (Rowell and Chadwick, 2018). CanESM2 exhibits lower frequency CAB detection rates than the other models, suggesting that it may struggle to represent the feature. The biases of the spatial distribution of the CAB in these climate models relative to ERA-5 reanalysis, and their significance relative to natural variability over the 30-year time period, are shown in Supplementary Figure S2. Overall, climate models exhibit biases that are larger than the variability across the reanalysis products. However, the reanalysis products do display some differences, particularly in the locations of peak CAB detection.

There is much more variability in the representation of the KD in CMIP5 models. BNU-ESM shows a very persistent KD, while CSIRO-Mk3.6 and GFDL models represent it reasonably well and some other models, such as CNRM-CM5 and CanESM2 miss it completely. Meanwhile, MERRA-2 shows a more infrequent KD than the other reanalysis products. We conclude that the KD is not as well represented in CMIP5 models as the CAB, and postpone further analysis for a future study.

We next study the seasonal cycle of key CAB features in the CMIP5 models. The seasonal cycles of the CAB latitude, frequency and extent in CMIP5 models and low resolution reanalysis products are shown in Figure 5. The CAB latitude and extent are both calendar day climatological means between 1970 and 2000, and all variables have been smoothed by a 2-week running mean. The extent is calculated by counting the total number of CAB grid cells on a given climatological day of the year. Only the days when a CAB was identified were used in the average. This gives an approximate measure of the lateral extent of the CAB, though it is not precisely comparable across CABs of different orientations. The latitude shown is the mean latitude of all CAB points on a given day, and the frequency is the proportion of days at a given time of year where a CAB is present.

Howard and Washington (2019) found that based on ERA-5 reanalysis, the CAB moves steadily southward between the start of August and the end of November, and that its detection frequency drops from near 100% at the start of October through to 10-20% at the beginning of December. In the present study, similar behavior is present in the latitude and frequency (the top and center panels respectively of Figure 5). The rate at which the CAB moves south is close to constant across models and consistent with ERA-5, at roughly 2 degrees per month. Results from ERA-5 are located at the southern edge of the CMIP5 simulated range. At any given time of the year, the climatological CAB latitude has a range of 5°. Since this range is of a similar order of magnitude to

the Nyquist frequency ($2\Delta x = 4°$), we surmise that the CAB latitude is represented in these models as well as can be expected. Based on the center panel of Figure 5, it is evident most models, as well as the MERRA-2 reanalysis, show a decreased CAB frequency in August, however all models except CAN-ESM2 recover by early September and the vast majority possess CABs that are present 80% of the time. The CAB breaks down between October and December in all models, with ERA-5 breaking down later than the ensemble mean but being located well within the model range. The ensemble mean CAB extent peaks at the beginning of October, consistent with the discontinuity width presented by Howard and Washington (2019) (their Figure 5). The reanalysis spread in the seasonal cycles of these metrics is approximately half of the model spread.

Based on the above analysis we conclude that the CAB is well represented in most of the climate models considered, with the exception being CanESM2. We therefore proceed to study the change in the CAB between present day and future climate models, and to assess the impact of this change on rainfall in southern Africa under the RCP8.5 scenario.

b. Future Change and Rainfall Implications

In this section, we explore how the CAB changes in the future and whether these changes are linked to projected southern African drying. Figure 6 shows the difference, in each model, between the CAB latitude, frequency and extent in the RCP8.5 end of 21st century simulation and in the historical end of 20th century simulation. The main change is an increase in the CAB frequency from October to December, peaking at approximately 25% in GFDL-CM3 and averaging to 13% in the ensemble mean. This frequency increase is accompanied by a northward shift in CAB latitude on average of 0.7°. These changes are significant relative to natural variability in between 11 and 15 of the 18 models across the three months, as shown in the bottom panel of Figure 6. This indicates that the gradual southward progression and seasonal frequency decline of the CAB

is delayed in most climate models, and so the CAB becomes more frequent towards the end of the season. Further analysis (not shown) indicates that the delay in CAB breakdown is approximately half a month. During this period, there is an increase in the CAB extent, which is significantly different from 0 as compared to model spread at the $p < 0.05$ level in November and December, and compared to natural variability in 12 models.

CAB frequency is also decreased in mid-August in most models and the ensemble mean. This is the same period when the CAB frequency was not well represented in Figure 5. This frequency decline may be related to the anomalous representation of the CAB in August. Most models return to displaying historical CAB frequencies by September, with the exception of CanESM2, whose CAB was shown earlier to be poorly represented in historical simulations.

Howard and Washington (2019) found that the interannual CAB frequency was anti-correlated with precipitation between 10° and 15°S in October, November and December. Since the October-December CAB frequency increases in most CMIP5 models considered in this study, it seems plausible that this increase may be linked to the projected rainfall decline present in most models. In order to explore this further, we decompose daily OND rainfall at each grid-cell into three components:

1. North of CAB rain: rain that fell at a grid-cell that was in the same longitude band as an identified CAB dryline, with the grid-cell located to the north of the dryline;

2. South of CAB rain: rain that fell at a grid-cell that was in the same longitude band as an identified CAB dryline, with the grid-cell located to the south of the dryline; and

3. CAB breakdown rain: rain that fell at a grid-cell for which no CAB drylines were detected in the same longitude band.

The top row of Figure 7 shows the decomposition of the historical climatological mean OND rainfall into these three categories, as a function of latitude and averaged over longitudes between 20° and 30°S. As predicted, the rainfall to the south of the CAB is small, and is only comparable to the total rainfall at subtropical latitudes (30°-40°S). Rainfall at tropical latitudes, between 0° and 15°S, is evenly distributed between the remaining two categories. North of CAB rainfall is identically zero south of 18°S, as the CAB does not extend south of this point.

The division of rainfall into these three components is based on the hypothesis, proposed by Howard and Washington (2019), that the CAB largely prevents tropical rain to its south and that the primary means by which spring rainfall occurs in southern Africa is a full or partial breach in the CAB. Thus component (2) - rainfall south of the CAB - is expected to be small and primarily of extra-tropical origin. The other components represent: (1) rainfall associated with 'Congo Air' in the deep tropics, and (3) rainfall associated with tropical temperate troughs (TTTs) and other CAB breakdown events. This decomposition does not account for the fact that a grid cell associated with an elongated TTT may exist to the south of a CAB grid cell due to the TTT's diagonal structure. However, this limitation does not appear to be significant, based on the calculated low magnitude of rain to the south of the CAB in Figure 7.

Meanwhile, the middle panel of Figure 7 shows the future change of each category of rainfall. The change in the total rainfall shows the familiar dipole structure, with most models showing drying south of 10°S and either wetting or a comparatively low magnitude of drying north of 5°S. The decomposition into rainfall classifications is enlightening: there is an increase in rainfall to the north of the CAB, and a decrease in rainfall coming from the CAB breakdown events. In each case the direction of change is remarkably robust between models and across latitudes.

To provide further visualisation of the projected change, the lower panel of Figure 7 shows the envelopes indicating the model spread of rainfall projections in historical (blue) and RCP8.5

(red) simulations. Change in the rainfall decomposition terms is more pronounced than change in the total rainfall. The green line in these figures indicates the number of models which show a significant change relative to natural variability. At least 13 of the 18 models show a significant decline in CAB breakdown rainfall between 8° and 28° S.

This implies that the ensemble mean OND drying and rainfall change dipole is associated with the change in the CAB frequency. The drying is fully contained within the component of the rainfall that falls on CAB breakdown days, while the wetting occurs to the north of the CAB. The rainfall rate per CAB break-down day and or north of CAB rainfall per CAB day was also considered, but no consensus on the sign of change was apparent (not shown). The projected decrease in rainfall on non-CAB days and increase in rainfall to the north of the CAB is therefore directly linked to the projected increase in the frequency of CAB days. The spatial patterns of the ensemble mean change of OND rainfall under this decomposition, shown in the top row of Figure 8, are consistent with this conclusion.

Furthermore, inter-model spread of the projected CAB frequency increase explains a large proportion of the projected southern African drying. This is shown in the lower panels of Figure 8, which show the inter-model regression of OND model rainfall change (averaged over 15° - 30°E and 5° - 25°S) against the modelled CAB frequency change. CAB frequency change is averaged over November and December, the months in which the ensemble mean change is significant. Before the CAB rainfall decomposition is applied, 46% of the inter-model variation of total OND rainfall change is explained by inter-model variation in the CAB frequency change. Variation in the rainfall decline during CAB breakdown events is more strongly predicted by variation in the CAB latitude change (R^2=0.71). While the CanESM2 data point (blue-green circle) appears to have a large degree of leverage in these regressions, its exclusion did strongly not impact the significance of the results (not shown).

Taken together, these results imply that the OND rainfall decline signal in southern Africa is largely explained by the increased frequency of the CAB, which prevents CAB breakdown associated rainfall in the regions that are located to the south of the CAB. Between 5° and 15°S, this comes with an increase in rainfall on CAB days, as parts of this region are often located to the north of the CAB.

4. Tropical lows

We now shift focus to tropical lows, cyclonic vortices that form in the Austral summer and have been found to deliver 31% of summer rainfall to the tropical edge region (16°- 22°S) of southern Africa (Howard et al., 2019). Tropical lows tend to cluster in Angola and western Zambia, where they form the synoptic expression of the late-summer tropical low phase of the climatological Angola low (Howard and Washington, 2018). This section first examines the representation of tropical lows in 18 CMIP5 models. We then consider their contribution to precipitation and future change.

a. Representation in Historical Climate Models

In order to evaluate the representation of tropical lows in CMIP5 models, we first consider climatological spatial distributions of tropical low locations, shown in Figure 9. From this figure, it is evident that most models get the broad shape of the distribution of tropical lows correct, with a maximum occurring in eastern Angola, the locus of the Angola tropical low. There is a wide range in the number of strong tropical low events per year. Most models show a lower count of tropical low days per year than the MERRA2 and ERA-5 reanalyses, while ERA-Interim is roughly in the middle of the model distribution. This stands in contrast to the findings of Munday and Washington (2017), who report that the geopotential height anomaly associated with the Angola low

is over-represented in CMIP5 models, although they did not consider ERA-5 or MERRA-2 for comparison. However, we do find that two models that have the most prevalent tropical lows (ACCESS1.3 and GFDL-ESM2G) also had strong geopotential height anomalies according to Munday and Washington (2017). The spread of tropical low characteristics between the three reanalysis products was studied in detail by Howard et al. (2019), and is typically reduced compared to the model spread.

The tropical low latitudes are shifted overly southwards towards the western edge of the Namibian Caprivi strip (18°S, 20°E) in most models, notably BNU-ESM, CNRM-CM5, inmcm4, NorESM1-M and HadGEM2-CC. The number of tropical lows per day is notably low in IPSL-CM5A-LR and inmncm4. BNU-ESM and HadGEM2-ES show an overly strong peak at 20°E, with very few tropical lows occurring outside the location of the Angola peak. For BNU-ESM, this is also clear from Figure 3, where the track longitudes are largely confined to 18° - 23°E. The biases of the spatial distribution of tropical lows in these climate models relative to ERA-5 reanalysis, and their significance relative to natural variability over the 30-year time period, are shown in Supplementary Figure S3.

Figure 10 shows the normalized distributions of four key properties of tropical lows: their longevities, latitudes, zonal velocities and T63 filtered vorticity. The southward shift of the tropical lows in CMIP5 models as compared to reanalysis is more clear from the latitude distribution sub-plot. Based on the distributions of longevity and zonal velocity, models may be divided into two groups: those with relatively more short-lived (<8 days) and relatively fewer long-lived tropical lows (10-20 days) than the reanalysis products, and those with fewer short-lived and more long-lived tropical lows. Those models in the first category tend to have a wider distribution of zonal velocities, with faster track speeds, while those in the second category have a greater proportion of stationary lows concentrated around 0 m/s. The first category therefore contains a greater

proportion of transient events that move off into the Atlantic Ocean, and the second contains a greater proportion of stationary Angola tropical lows. Typical extreme cases for each category are CNRM-CM5 and GFDL-ESM2G. Examining Figure 3 reveals a consistent story: for the case study year CNRM-CM5 is dominated by transient events (diagonal lines) while GFDL-ESM2G contains 4-5 long-lived events that meander across the continent and are frequency stationary, as well as some smaller events that are both stationary and transient. The distributions of the filtered vorticity largely follow that of reanalysis. Biases in all these quantities are significant relative to natural variability in at least 12 out of the 17 models considered.

The top right panel of Figure 10 shows the number of tropical low days per year. This metric reflects the overall magnitude of the signal in Figure 3 discussed earlier. The models with the lowest values (IPSL-CM5A-LR and inmcm4) also show a higher proportion of tropical lows just below the vorticity cut-off in the lower left panel of Figure 10.

Rainfall is attributed to tropical lows under the assumption that all rainfall that falls within 5 degrees of the centroid of a tropical low is associated with that tropical low. Rainfall is decomposed into a tropical low portion and a remainder portion. Howard et al. (2019) found that 70% of rainfall in south west Angola and 31% of rainfall across the tropical edge region (16° - 22 °S) was attributable to tropical lows. The spatial pattern of rainfall attribution for CMIP5 models is shown in Figure 11, and the overall proportion of rainfall attributed to tropical lows in each model between 15° - 30°E and 10° - 25°S is shown in the lower right panel of Figure 10. We find that approximately 30% - 60% of rainfall over southern Africa is associated with tropical lows between these latitudes. The spatial patterns of rainfall attribution match well with those found by Howard et al. (2019) (reproduced here in lower panels of Figure 11). The biases of these spatial patterns relative to ERA-5 reanalysis, and their significance relative to natural variability over the 30-year time period, are shown in Supplementary Figure S4.

There are some differences between tropical lows in reanalysis products and in CMIP5 models, including latitude and longevity distributions, and there is a wide distribution across models in the mean number of strong tropical low days per year. However, tropical lows are consistently present in each model with key statistics varying by less than 20%. We therefore conclude that they are sufficiently resolved to examine projected tropical low changes and how those changes impact southern African precipitation projections.

b. Future Change and Rainfall Implications

The overall trend in the spatial distribution of tropical lows between end of 21st century RCP8.5 and end of 20th century historical simulations is a decrease in tropical low frequency and in some cases a northward shift, as is shown in Figure 12. Some models, including ACCESS1.0, HadGEM2-CC, HadGEM2-ES and GFDL-CM3, show a sharp decline in tropical lows exceeding 1 tropical low day per $2^\circ \times 2^\circ$ box per year that is restricted to the location of the peak of their historical tropical low locations. Northward shifts are evident in CanESM2, IPSL-CM5A-LR and MPI-ESM-LR. Only MPI-ESM-MR shows an increase in tropical low frequency. Despite many models showing similar overall patterns in tropical low decline, the spatial pattern of change and the location of statistically significant changes varies widely across the models. The ensemble mean exhibits an overall 15% decline in the number of tropical low days that occur in each year.

Correspondingly, the spatial pattern of rainfall change between December and February, the main tropical low months, shows a high degree of variation between models, consistent with Lazenby et al. (2018). Filled green and purple contours show wetting and drying of the overall seasonal mean rainfall in each model in Figure 13. These are overlain by contours, in black and red, of the wetting and drying of the component of the rainfall attributed to tropical lows. Changes which were not significant compared to natural variability at a $p < 0.05$ level were masked. It is

evident that all the land-based local maxima and minima of total rainfall change located between 10° and 25°S correspond to an associated maxima or minima in tropical low rainfall change. Comparing with Figure 12, these changes correspond with spatial changes in the frequency of tropical lows.

The ensemble mean tropical low rainfall change in this region (Figure 13, lower right panel) also corresponds to the ensemble mean tropical low spatial distribution change (Figure 12, lower right panel), with a decrease along 18°S centered south east Angola and an increase further north. The spatial pattern of total rainfall decline maps accurately onto the spatial pattern of tropical low rainfall decline in southern Angola and northern Namibia. However, the rainfall increase to the north of this region has its maximum further north in the Congo and is likely delivered by other synoptic systems.

In order to quantify the relationship between changes in rainfall and tropical low frequency, the Pearson's r coefficient of the spatial correlation between projected rainfall change and tropical low frequency change between 5° - 25°S for all land points is shown in the top row of Figure 14. The correlation for overall rainfall is low (typically 0.1 - 0.3) but consistently positive in all but two models. The correlation for the tropical low rainfall component is higher, with values averaging around 0.4. There is no consistent signal in the direction of correlation between the remaining rainfall pattern change and the tropical low distribution change. In this manner, the divergence in model rainfall projections in DJF over tropical southern Africa is linked to the uncertainty in the spatial response of tropical lows to climate change.

Averaging over land points in the region from 5° - 25°S, the projected frequency change in tropical lows is a good predictor of the inter-model spread of rainfall change (r=0.58, p=0.015). This is indicated in the regression shown in Figure 14 (lower left panel). The decomposition into rainfall associated with tropical lows and a remainder component (lower center and right panels

of Figure 14) indicates that this influence of tropical lows is direct, as the change in tropical low rainfall is significantly correlated with the change in tropical lows, and the change in the remainder term is not. Therefore, the spread in future projections of tropical lows is a major contributor to the spread of rainfall predictions in DJF over southern Africa.

5. Discussion

a. Remarks on the Congo Air Boundary

We have found that the CAB is well represented in CMIP5 models, and that its projected frequency increase is able to distinguish between models that show strong and weak declines in OND rainfall south of 10°S. In this section, we discuss the implications of the historical representation of the CAB, and compare our results to other studies of the OND rainfall decline.

The accuracy of historical representation of the CAB in CMIP5 models is reasonable, despite the perpendicular width of the CAB being of order 100 km (Howard and Washington, 2019), below the resolution of most CMIP5 models. The southward displacement of the CAB between August and December is roughly 8 degrees of latitude, which in the coarsest models is equivalent to 4 grid cells, and yet the rate of the CAB's progression is very similar across models. This suggests that representation of the CAB, and its seasonal progression, is controlled by a process that climate models do not struggle to simulate, and so is not controlled by processes that act at the grid box scale. As with the tropical rainbelt globally, the seasonal progression is clearly associated with the progression of the latitude of maximum solar insolation. Meanwhile, the sharp gradients in humidity bring to mind bifurcations into dry and moist convective states observed in idealized radiative convective equilibrium models (e.g., Emanuel et al., 2014).

We have found that projections of CAB frequency have different consequences north and south of the climatological CAB. The relationship between the CAB frequency and rainfall south of the CAB's climatological position is an intuitive one. In this region, saturation is rarely achieved when the CAB is present, unless extra-tropical processes dominate. Most rainfall comes from CAB breakdown events. When the gradual seasonal CAB breakdown is delayed, as in the future model projections, there are fewer rainy days in this region, and hence less rain. Meanwhile, there is an overall increase in rainfall to the north of the climatological CAB. However, this increase is not limited to the location of the CAB, as OND rainfall is projected to increase across much of equatorial Africa (Creese et al., 2019). Therefore, there is a consistent projected increase in rainfall in locations that are generally located the north of the CAB, but this is not necessarily driven by the corresponding projected increase in CAB frequency. The contrasting impacts that the CAB frequency has to its north and south are important for determining the precise location of projected rainfall decline. Rainfall to the south of the mean CAB position is projected to decline due to the projected increase in CAB frequency, while rainfall to the north is projected to increase. Therefore, the CAB may be expected to set the location of the boundary of rainfall decline.

The work presented here is consistent with previous studies of rainfall projections over southern Africa. Dunning et al. (2018) found that the seasonal progression of the African rain belt is tied up in the strengths of the Saharan and Angola heat lows, both of which are projected to intensify in a warmer world. Munday and Washington (2019) found a similar result, that models with a deeper future Angola heat low showed a higher intensity of drying, while Cook and Vizy (2013) observed a strengthening of the heat low in regional climate model simulations. The Angola heat low is intrinsically linked to the CAB (Howard and Washington, 2019), being consistently located approximately 1° south of the CAB and sharing circulation features. Therefore an increase in the climatological CAB frequency corresponds to an increase in the heat low intensity.

By applying the Chadwick et al. (2013) decomposition, Lazenby et al. (2018) attributed the OND rainfall change to dynamic rather than thermodynamic changes, associated with spatial shifts in the pattern of convective mass fluxes. In the context of this methodology, it is useful to consider the atmosphere to the north of the CAB and during CAB breakdown events as capable of deep convection, and to the south of the CAB as incapable of deep convection. The increased CAB frequency corresponds to a decrease in the proportion of the time that convection may occur in the region south of 10°S, and so is associated with a shift in deep convection away from southern Africa.

Figures 3(f-g) in Lazenby et al. (2018) also demonstrated that there was a decrease in near surface relative humidity between 10° and 20°S, but that this did not contribute to the overall precipitation change budget. This finding underscores the fundamental concept outlined by the CAB: that the southern African atmosphere during the Austral spring is often characterized at any instant by a dichotomy of states: one that is severely moisture limited and one that is close to saturated, with very little in between (Howard and Washington, 2019). In such a scenario, small thermodynamic perturbations have less potential to change the likelihood of convection than small dynamical perturbations. This is because a dynamical perturbation may move the moist airmass into, or away from a given location, drastically changing the likelihood of convection at that spot. Meanwhile, a small change in saturation temperature is unlikely to change the likelihood of convection if the atmosphere is either severely dry or not at all moisture limited.

b. Remarks on Tropical lows

Uncertainty in future projections of tropical lows in southern Africa has been identified as a source of the uncertainty and broad model spread in rainfall projections in this region during the

main rainy season. This uncertainty derives from variations in the changes of the climatological tropical low spatial distribution, however some robust changes are present, as discussed below.

The historical spatial distribution of tropical lows features a southward bias as compared to reanalysis. Models show a greater proportion of tropical lows centered near 18°S and too few located around 15°S. This bias is consistent with other studies of the historical CMIP5 rainfall bias over southern Africa. An interannual southward shift in the Angola low has been associated with an increase in rainfall over subtropical southern Africa (Pascale et al., 2019; Crétat et al., 2018), consistent with the direction of the rainfall bias (Lazenby et al., 2016). Furthermore, Munday and Washington (2017) found a correlation between the magnitude of this wet bias and the strength of the Angola low, which they found was overly intense in most models. They also found that the climatological position of the Angola low was shifted towards the Angola-Namibia border in many models.

Despite differences in the patterns, there is a consensus in all but one model of overall tropical low decline south of 15°S. This is reflected in the ensemble mean of both precipitation and tropical low location shifts. A large minority of models also show a marked increase in tropical lows north of this line, signifying a northward shift. However, this change is less robust than the decline further south. A northward shift and overall decline of tropical low location mirrors the characteristic response of tropical lows to El Niño events (Howard et al., 2019; Pascale et al., 2019).

Lazenby et al. (2018) proposed that the diverse range of future projections in DJF is associated with inter-model differences in the SST changes in the Indian and Atlantic Oceans. Since interannual variability of the Angola low, which in late summer is the climatological expression of tropical lows, is sensitive to SSTs in these oceans (Pascale et al., 2019), it is likely that variability in SST projections may lead to variability in tropical low distributions, which in turn lead to the spread of projected rainfall changes.

6. Conclusion

The CMIP5 ensemble predicts a drying trend in both spring and summer in southern Africa. Spring drying is robust across all models, and is associated with a delay in the wet season onset (Dunning et al., 2018). Such delays would cause a shortening of the growing season, impacting regional agriculture and food security (Lobell et al., 2008; Schlenker and Lobell, 2010). Model projections in the summer are more divergent and the ensemble mean drying trend in this season is less robust. However, rainfall changes in this season would be equally disruptive to the local economy. For this reason, it is imperative that the mechanisms of future rainfall change demonstrated by CMIP5 models are well understood.

The present study has placed the spring and summer projected rainfall change in the context of two classes of weather events, tropical lows and the CAB. These features are predominant in each respective season and are sufficiently well resolved in the climate models. By doing so, we have attributed model consensus on spring drying to increases in CAB frequency and latitude, and the lack of model consensus on summer rainfall change to uncertainty in the tropical low response to a warmer world. This work provides crucial context for the projected changes and grounds changes to the local climate in meteorological theory.

We have found that the spring drying trend is strongly correlated across models with an increased frequency in the CAB. This delayed breakdown causes an increase in its average frequency between October and December of approximately 13%. Model consensus on its projected change agree that the CAB will be located 0.5° - 1° further north and its gradual seasonal decline will occur half a month later at the end of 21st century than the 20th under the RCP8.5 scenario. These changes are significant as against internal variability in 12 - 15 of the 18 models. Therefore, we

strongly advocate for further research into this understudied feature of the climate system, particularly in the form of observational field campaigns.

Tropical lows, which make up the synoptic expression of the Angola low in the southern African summer, show more model spread in their future change, particularly when considering small-scale spatial shifts. This increased model uncertainty is a contributor to the divergence of DJF rainfall projections in southern Africa. However, despite spatial differences, a statistically significant decline in tropical low frequency south of 15°S is present in 11 models, with an overall ensemble mean decline of 10%. The response of tropical lows to future warming will be important for rainfall change in this region.

Acknowledgments. This work has been generously supported by the Origin Foundation John Monash Scholarship and by the Future Climate for Africa UMFULA project, with financial support from the U.K. Natural Environment Research Council (NERC), NE/M020207/1, and the U.K. Government's Department for International Development (DfID). The GCM data used in this study were made available through the Earth System Grid Federation (ESGF) Peer-to-Peer system (`https://pcmdi.llnl.gov/search/cmip5/`). Reanalysis data used in this analysis were provided by the Copernicus Climate Change Service (`https://cds.climate.copernicus.eu/cdsapp#!/home`), the European Centre for Medium Range Weather Forecasts (`https://apps.ecmwf.int/datasets/data/interim-full-daily/levtype=pl/`) and NASA (`https://disc.sci.gsfc.nasa.gov/daac-bin/FTPSubset.pl`). Color maps were sourced from cmocean (`https://matplotlib.org/cmocean/`). We thank Kevin Hodges for access to TRACK and Paul-Arthur Monerie for assistance regarding decadal variability.

References

Aloysius, N. R., J. Sheffield, J. E. Saiers, H. Li, and E. F. Wood, 2016: Evaluation of historical and future simulations of precipitation and temperature in central Africa from CMIP5 climate models. *Journal of Geophysical Research: Atmospheres*, **121 (1)**, 130–152, doi: 10.1002/2015JD023656, URL http://doi.wiley.com/10.1002/2015JD023656.

Baray, J., S. Baldy, R. Diab, and J. Cammas, 2003: Dynamical study of a tropical cut-off low over south africa, and its impact on tropospheric ozone. *Atmospheric Environment*, **37 (11)**, 1475 – 1488, doi:https://doi.org/10.1016/S1352-2310(02)00999-8, URL http://www.sciencedirect.com/science/article/pii/S1352231002009998.

Bengtsson, L., K. I. Hodges, M. Esch, N. Keenlyside, L. Kornblueh, J. J. Luo, and T. Yamagata, 2007: How may tropical cyclones change in a warmer climate? *Tellus, Series A: Dynamic Meteorology and Oceanography*, **59 A (4)**, 539–561, doi:10.1111/j.1600-0870.2007.00251.x, URL https://doi.org/10.1111/j.1600-0870.2007.00251.x.

Canny, J., 1986: A Computational Approach to Edge Detection. *IEEE Transactions on Pattern Analysis and Machine Intelligence*, **8 (6)**, 679–698, doi:10.1109/TPAMI.1986.4767851, URL https:doi.org/10.1109/TPAMI.1986.4767851.

Chadwick, R. S., I. Boutle, and G. Martin, 2013: Spatial patterns of precipitation change in CMIP5: Why the rich do not get richer in the tropics. *Journal of Climate*, **26 (11)**, 3803–3822, doi:10.1175/JCLI-D-12-00543.1, URL https://journals.ametsoc.org/doi/10.1175/JCLI-D-12-00543.1.

Chou, C., J. D. Neelin, C. A. Chen, and J. Y. Tu, 2009: Evaluating the "rich-get-richer" mechanism in tropical precipitation change under global warming. *Journal of Climate*, **22 (8)**,

1982–2005, doi:10.1175/2008JCLI2471.1, URL https://journals.ametsoc.org/doi/pdf/10.1175/2008JCLI2471.1.

Conway, D., and Coauthors, 2015: Climate and southern Africa's water-energy-food nexus. *Nature Climate Change*, **5 (9)**, 837–846, doi:10.1038/nclimate2735, URL https://doi.org/10.1038/nclimate2735.

Cook, C., C. J. Reason, and B. C. Hewitson, 2004: Wet and dry spells within particularly wet and dry summers in the South African summer rainfall region. *Climate Research*, **26 (1)**, 17–31, doi:10.3354/cr026017, URL https://doi.org/10.3354/cr026017.

Cook, K. H., and E. K. Vizy, 2013: Projected changes in East African rainy seasons. *Journal of Climate*, **26 (16)**, 5931–5948, doi:10.1175/JCLI-D-12-00455.1, URL https://doi.org/10.1175/JCLI-D-12-00455.1.

Creese, A., R. Washington, and C. Munday, 2019: The Plausibility of September–November Congo Basin Rainfall Change in Coupled Climate Models. *Journal of Geophysical Research: Atmospheres*, **124 (11)**, 5822–5846, doi:10.1029/2018JD029847, URL https://onlinelibrary.wiley.com/doi/abs/10.1029/2018JD029847.

Crétat, J., B. Pohl, B. Dieppois, S. Berthou, and J. Pergaud, 2018: The Angola Low: relationship with southern African rainfall and ENSO. *Climate Dynamics*, **52 (4)**, 1783–1803, doi:10.1007/s00382-018-4222-3, URL https://doi.org/10.1007/s00382-018-4222-3.

Dare, R. A., N. E. Davidson, and J. L. McBride, 2012: Tropical Cyclone Contribution to Rainfall over Australia. *Monthly Weather Review*, **140 (11)**, 3606–3619, doi:10.1175/MWR-D-11-00340.1, URL https://journals.ametsoc.org/doi/10.1175/MWR-D-11-00340.1.

691 Dunning, C. M., E. C. Black, and R. P. Allan, 2018: Later wet seasons with more intense rainfall
692 over Africa under future climate change. *Journal of Climate*, **31 (12)**, JCLI–D–18–0102.1, doi:
693 10.1175/JCLI-D-18-0102.1, URL https://doi.org/10.1175/JCLI-D-18-0102.1.

694 Emanuel, K., A. A. Wing, and E. M. Vincent, 2014: Radiative-convective instability. *Journal of*
695 *Advances in Modeling Earth Systems*, **6 (1)**, 75–90, doi:10.1002/2013MS000270, URL https:
696 //doi.org/10.1002/2013MS000270.

697 Hachigonta, S., C. J. Reason, and M. Tadross, 2008: An analysis of onset date and rainy season
698 duration over Zambia. *Theoretical and Applied Climatology*, **91 (1-4)**, 229–243, doi:10.1007/
699 s00704-007-0306-4, URL https://doi.org/10.1007/s00704-007-0306-4.

700 Held, I. M., and B. J. Soden, 2006: Robust Responses of the Hydrological Cycle to Global Warm-
701 ing. *Journal of Climate*, **19 (11)**, 5686–5699, URL https://journals.ametsoc.org/doi/10.1175/
702 JCLI3990.1.

703 Hodges, K. I., 1994: A General Method for Tracking Analysis and its Applica-
704 tion to Meteorological Data. *Monthly Weather Review*, **122 (11)**, 2573–2586, doi:
705 10.1175/1520-0493(1994)122⟨2573:AGMFTA⟩2.0.CO;2, URL https://doi.org/10.1175/
706 1520-0493(1994)122⟨2573:AGMFTA⟩2.0.CO;2.

707 Hodges, K. I., 1999: Adaptive Constraints for Feature Tracking. *Monthly Weather Review*,
708 **127**, 1362–1373, doi:10.1175/1520-0493(1999)127⟨1362:ACFFT⟩2.0.CO;2, URL https://doi.
709 org/10.1175/1520-0493(1999)127⟨1362:ACFFT⟩2.0.CO;2.

710 Hodges, K. I., A. Cobb, and P. L. Vidale, 2017: How well are tropical cyclones represented in
711 reanalysis datasets? *Journal of Climate*, **30 (14)**, 5243–5264, doi:10.1175/JCLI-D-16-0557.1,
712 URL https://doi.org/10.1175/JCLI-D-16-0557.1.

Howard, E., and R. Washington, 2018: Characterizing the synoptic expression of the angola low. *Journal of Climate*, **31 (17)**, 7147–7165, doi:10.1175/JCLI-D-17-0017.1, URL https://doi.org/10.1175/JCLI-D-18-0017.1.

Howard, E., and R. Washington, 2019: Drylines in Southern Africa: Rediscovering the Congo Air Boundary. *Journal of Climate*, **32**, 8223–8242, URL https://doi.org/10.1175/JCLI-D-19-0437.1.

Howard, E., R. Washington, and K. I. Hodges, 2019: Tropical lows in southern Africa: tracks, rainfall contributions and the role of ENSO. *Journal of Geophysical Research: Atmospheres (in press)*.

James, R., and R. Washington, 2013: Changes in African temperature and precipitation associated with degrees of global warming. *Climatic Change*, **117 (4)**, 859–872, doi:10.1007/s10584-012-0581-7, URL https://doi.org/10.1007/s10584-012-0581-7.

Jiang, Y., L. Zhou, C. J. Tucker, A. Raghavendra, W. Hua, Y. Y. Liu, and J. Joiner, 2019: Widespread increase of boreal summer dry season length over the congo rainforest. *Nature Climate Change*, **9**, 617–622, URL https://doi.org/10.1038/s41558-019-0512-y.

Khouakhi, A., G. Villarini, and G. A. Vecchi, 2017: Contribution of tropical cyclones to rainfall at the global scale. *Journal of Climate*, **30 (1)**, 359–372, doi:10.1175/JCLI-D-16-0298.1, URL https://journals.ametsoc.org/doi/10.1175/JCLI-D-16-0298.1.

Kniveton, D. R., R. Layberry, C. J. R. Williams, and M. Peck, 2009: Trends in the start of the wet season over Africa. *International Journal of Climatology*, **29 (9)**, 1216–1225, doi:10.1002/joc.1792, URL https://rmets.onlinelibrary.wiley.com/doi/abs/10.1002/joc.1792, https://rmets.onlinelibrary.wiley.com/doi/pdf/10.1002/joc.1792.

Lavender, S. L., and D. J. Abbs, 2013: Trends in Australian rainfall: Contribution of tropical cyclones and closed lows. *Climate Dynamics*, **40 (1-2)**, 317–326, doi:10.1007/s00382-012-1566-y, URL https://doi.org/10.1007/s00382-012-1566-y.

Lazenby, M. J., M. C. Todd, R. S. Chadwick, and Y. Wang, 2018: Future precipitation projections over central and Southern Africa and the adjacent Indian Ocean: What causes the changes and the uncertainty? *Journal of Climate*, **31 (12)**, 4807–4826, doi:10.1175/JCLI-D-17-0311.1, URL https://doi.org/10.1175/JCLI-D-17-0311.1.

Lazenby, M. J., M. C. Todd, and Y. Wang, 2016: Climate model simulation of the South Indian Ocean Convergence Zone: Mean state and variability. *Climate Research*, **68 (1)**, 59–71, doi:10.3354/cr01382, URL https://doi.org/10.3354/cr01382.

Leroux, M., 2001: *The climate of tropical Africa*, Vol. 3-9. Springer, 39–45 pp.

Lobell, D. B., M. B. Burke, C. Tebardi, M. D. Mastrandrea, W. P. Falcon, and R. L. Naylor, 2008: Prioritizing Climate Change Adaptation Needs for Food Security in 2030. *Science*, **319 (5863)**, 607–610, doi:10.1126/science.1152339, URL https://doi.org/10.1126/science.1152339.

Munday, C., and R. Washington, 2017: Circulation Controls on Southern African Precipitation in Coupled Models: The Role of the Angola Low. *Journal of Geophysical Research: Atmospheres*, **122**, 1–17, doi:10.1002/2016JD025736, URL https://doi.org/10.1002/2016JD025736.

Munday, C., and R. Washington, 2019: Controls on the diversity in climate model projections of early summer drying over Southern Africa. *Journal of Climate*, **32**, 3707–3725, doi:10.1175/JCLI-D-18-0463.1, URL http://journals.ametsoc.org/doi/10.1175/JCLI-D-18-0463.1.

Pascale, S., B. Pohl, S. B. Kapnick, and H. Zhang, 2019: On the Angola Low Interannual Variability and Its Role in Modulating ENSO Effects in Southern Africa. *Journal of Climate*, **32 (15)**, 4783–4803, doi:10.1175/jcli-d-18-0745.1, URL https://doi.org/10.1175/JCLI-D-18-0745.1.

Rastogi, D., M. Ashfaq, L. R. Leung, S. Ghosh, A. Saha, K. I. Hodges, and K. Evans, 2018: Characteristics of Bay of Bengal Monsoon Depressions in the 21st Century. *Geophysical Research Letters*, **45 (13)**, 6637–6645, doi:10.1029/2018GL078756, URL https://doi.org/10.1029/2018GL078756.

Reason, C. J., and D. Jagadheesha, 2005: A model investigation of recent ENSO impacts over southern Africa. *Meteorology and Atmospheric Physics*, **89 (1-4)**, 181–205, doi:10.1007/s00703-005-0128-9, URL https://doi.org/10.1007/s00703-005-0128-9.

Rowell, D. P., and R. S. Chadwick, 2018: Causes of the uncertainty in projections of tropical terrestrial rainfall change: East Africa. *Journal of Climate*, **31 (15)**, 5977–5995, doi:10.1175/JCLI-D-17-0830.1, URL http://journals.ametsoc.org/doi/10.1175/JCLI-D-17-0830.1.

Sardeshmukh, P. D., and B. J. Hoskins, 1988: The Generation of Global Rotational Flow by Steady Idealized Tropical Divergence. *Journal of the Atmospheric Sciences*, **45 (7)**, 1228–1251, doi:10.1175/1520-0469(1988)045⟨1228:TGOGRF⟩2.0.CO;2, URL https://doi.org/10.1175/1520-0469(1988)045⟨1228:TGOGRF⟩2.0.CO;2.

Scheff, J., and D. Frierson, 2012a: Twenty-First-Century multimodel subtropical precipitation declines are mostly midlatitude shifts. *Journal of Climate*, **25 (12)**, 4330–4347, doi:10.1175/JCLI-D-11-00393.1, URL https://doi.org/10.1175/JCLI-D-11-00393.1.

Scheff, J., and D. M. W. Frierson, 2012b: Robust future precipitation declines in CMIP5 largely reflect the poleward expansion of model subtropical dry zones. *Geophysical Research Letters*,

39 (17), 1–6, doi:10.1029/2012GL052910, URL https://doi.org/10.1029/2012GL052910.

Schlenker, W., and D. B. Lobell, 2010: Robust negative impacts of climate change on African agriculture. *Environmental Research Letters*, **5 (1)**, doi:10.1088/1748-9326/5/1/014010, URL https://doi.org/10.1088/1748-9326/5/1/014010.

Taljaard, J. J., 1953: The mean circulation in the lower troposphere over Southern Africa. *South African Geographical Journal*, **35 (1)**, 33–45, doi:10.1080/03736245.1953.10559299, URL https://doi.org/10.1080/03736245.1953.10559299.

Taljaard, J. J., 1972: Synoptic Meteorology of the Southern Hemisphere. *Meteorology of the Southern Hemisphere*, C. W. Newton, Ed., American Meteorological Society, Boston, chap. 8, 139–213.

Taljaard, J. J., 1986: Change of rainfall distribution and circulation patterns over Southern Africa in summer. *Journal of Climatology*, **6**, 579–592, URL https://doi.org/10.1002/joc.3370060602.

Torrance, J. D., 1979: Upper windflow patterns in relation to rainfall in South-East Central Africa. *Weather*, **34 (3)**, 106–115, doi:10.1002/j.1477-8696.1979.tb03418.x, URL https://doi.org/10.1002/j.1477-8696.1979.tb03418.x.

Van Heerden, J., and J. J. Taljaard, 1998: Africa and Surrounding Waters. *Meteorology of the Southern Hemisphere*, D. J. Karoly, and D. G. Vincent, Eds., American Meteorological Society, Easton, 141–174.

LIST OF TABLES

799 TABLE 1. List of CMIP5 models and reanalysis products considered in this study, together with horizontal
800 grid spacings, and an indication of whether the model was used to study the CAB, tropical lows (TL) or both.

Model Name	Institute	Horizontal Spacing	CAB	TL
bcc-csm1-1-m	Beijing Climate Center, China Meteorological Administration	$1.125^\circ \times 1.125^\circ$	1	1
BNU-ESM	College of Global Change and Earth System Science, Beijing Normal University	$2.8^\circ \times 2.8^\circ$	1	1
CanESM2	Canadian Centre for Climate Modelling and Analysis	$2.8^\circ \times 2.8^\circ$	1	1
CNRM-CM5	Centre National de Recherches Meteorologiques	$1.4^\circ \times 1.4^\circ$	1	1
ACCESS1-0	Commonwealth Scientific and Industrial Research Organisation and Bureau of Meteorology, Australia	$1.25^\circ \times 1.825^\circ$	1	1
ACCESS1-3	Commonwealth Scientific and Industrial Research Organisation and Bureau of Meteorology, Australia	$1.25^\circ \times 1.825^\circ$	1	1
CSIRO-Mk3-6-0	Commonwealth Scientific and Industrial Research Organisation in collaboration with Queensland Climate Change Centre of Excellence	$1.825^\circ \times 1.825^\circ$	1	
inmcm4	Institute for Numerical Mathematics, Moscow, Russia	$1.5^\circ \times 2.0^\circ$	1	1
IPSL-CM5A-LR	L'Institut Pierre-Simon Laplace	$1.9^\circ \times 3.75^\circ$	1	1
IPSL-CM5A-MR	L'Institut Pierre-Simon Laplace	$1.25^\circ \times 2.5^\circ$	1	1
IPSL-CM5B-LR	L'Institut Pierre-Simon Laplace	$1.9^\circ \times 3.75^\circ$	1	1
HadGEM2-CC	UK Met Office Hadley Centre	$1.25^\circ \times 1.9^\circ$	1	1
HadGEM2-ES	UK Met Office Hadley Centre	$1.25^\circ \times 1.9^\circ$	1	1

MPI-ESM-LR	Max Planck Institute for Meteorology M24	$1.8° \times 1.8°$		1
MPI-ESM-MR	Max Planck Institute for Meteorology M24	$1.8° \times 1.8°$		1
NorESM1-M	Norwegian Climate Centre	$1.875° \times 2.5°$	1	1
GFDL-CM3	NOAA/Geophysical Fluid Dynamics Laboratory	$2.0° \times 2.5°$	1	1
GFDL-ESM2G	NOAA/Geophysical Fluid Dynamics Laboratory	$2.0° \times 2.5°$	1	1
GFDL-ESM2M	NOAA/Geophysical Fluid Dynamics Laboratory	$2.0° \times 2.5°$	1	
CESM1-CAM5	Community Earth System Model contributor	$0.94° \times 1.25°$	1	
Reanalysis Name	Institute	Horizontal Spacing	CAB	TL
ERA-5	European Centre for Medium Range Forecasting	$0.25° \times 0.25°$	1	1
ERA-Interim	European Centre for Medium Range Forecasting	$0.75° \times 0.75°$	1	1
MERRA-2	NASA	$0.5° \times 0.75°$	1	1

LIST OF FIGURES

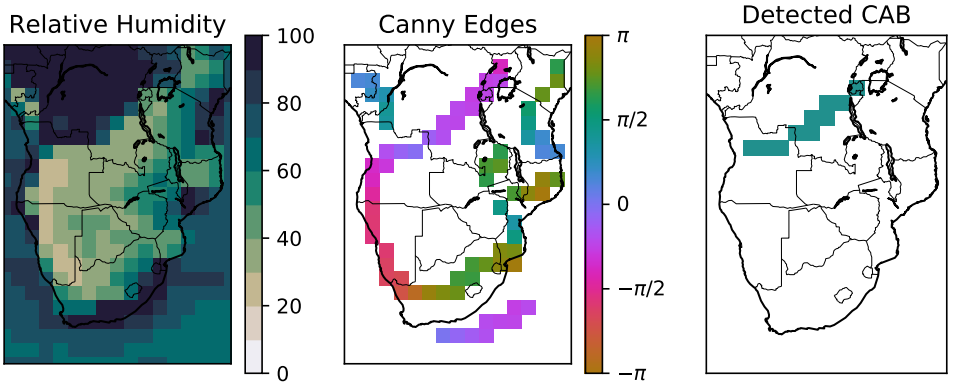

FIG. 1. Surface relative humidity (left panel), Canny edges (middle panel) and identified CAB locations (right panel) on the 9th of September 1999 in ACCESS1.3.

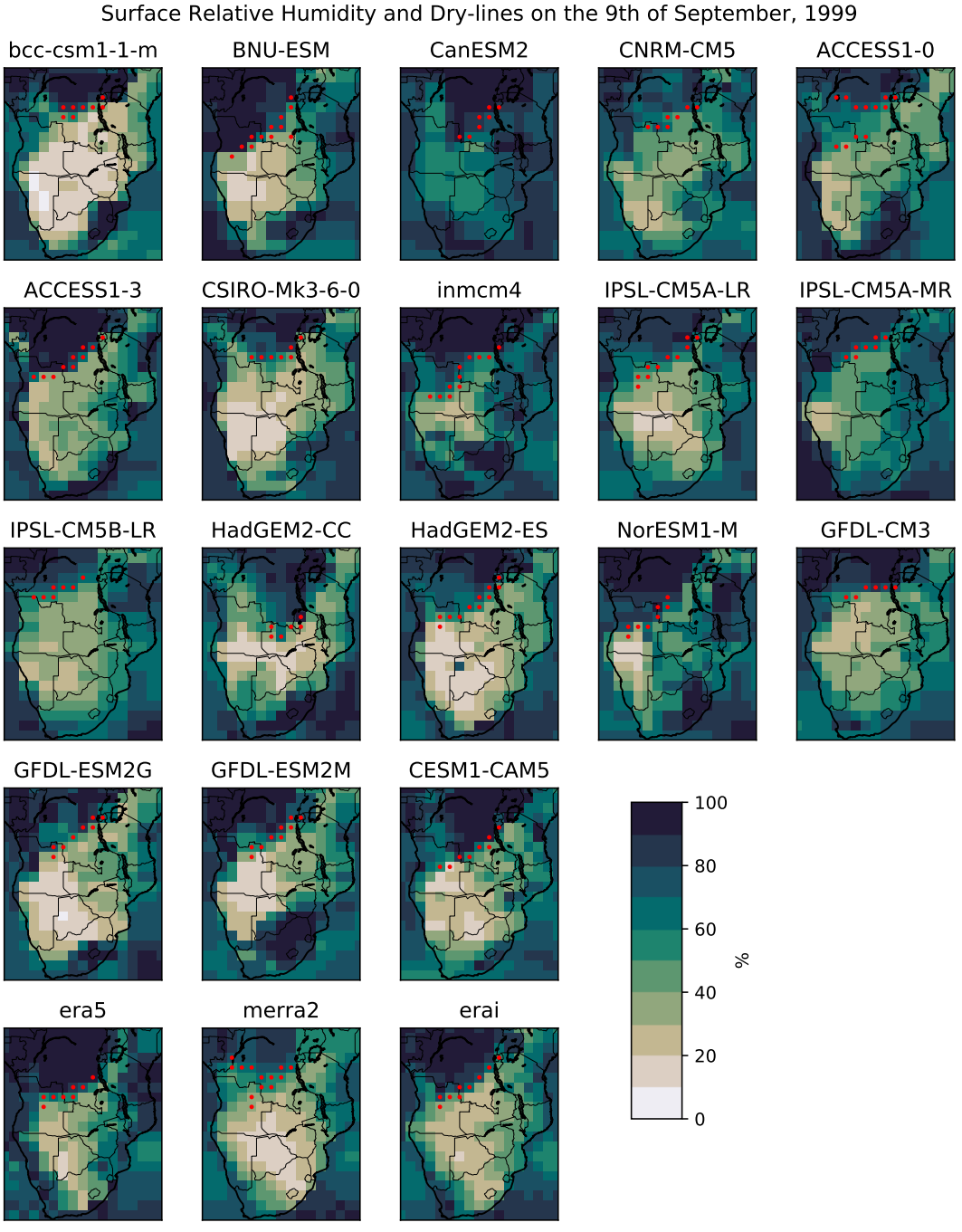

878 FIG. 2. Surface relative humidity (colors) and identified CAB locations (red dots) on the 9th of September
879 1999 in each model and reanalysis product. Surface humidity has been regridded to a $2° \times 2°$ grid using the
880 nearest neighbor method.

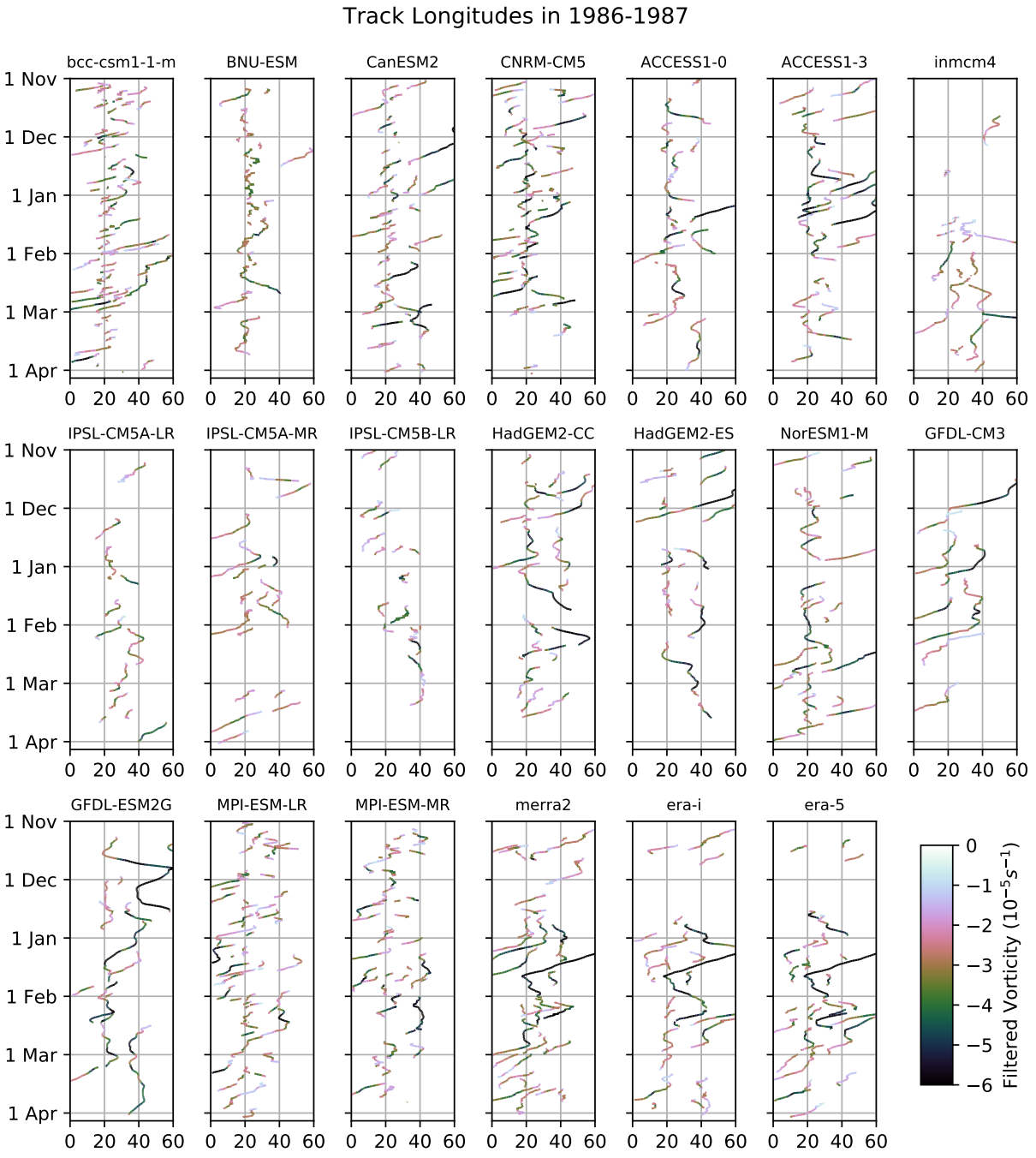

881 FIG. 3. Tropical low track Hovmöller plots for each model and reanalysis product. $x-$axis: longitude, $y-$axis:
882 time. Colors indicate the T63 filtered vorticity of the tropical low event, a measure of the event intensity.

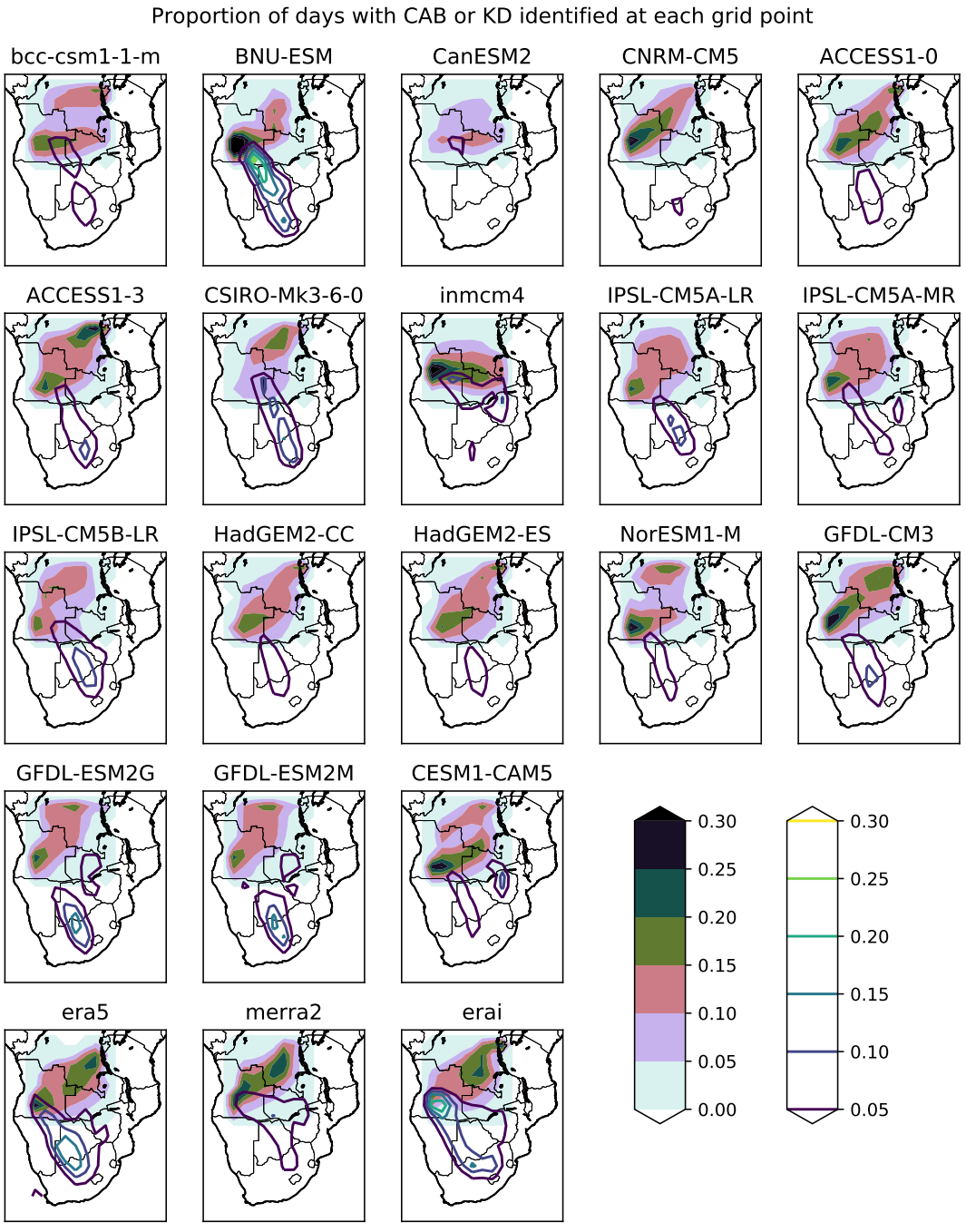

883 FIG. 4. Spatial distributions of CAB and KD frequency (number of events per interpolated grid cell per year).

884 Filled contours: CAB. Line contours: KD. Panels indicate different models and reanalysis products.

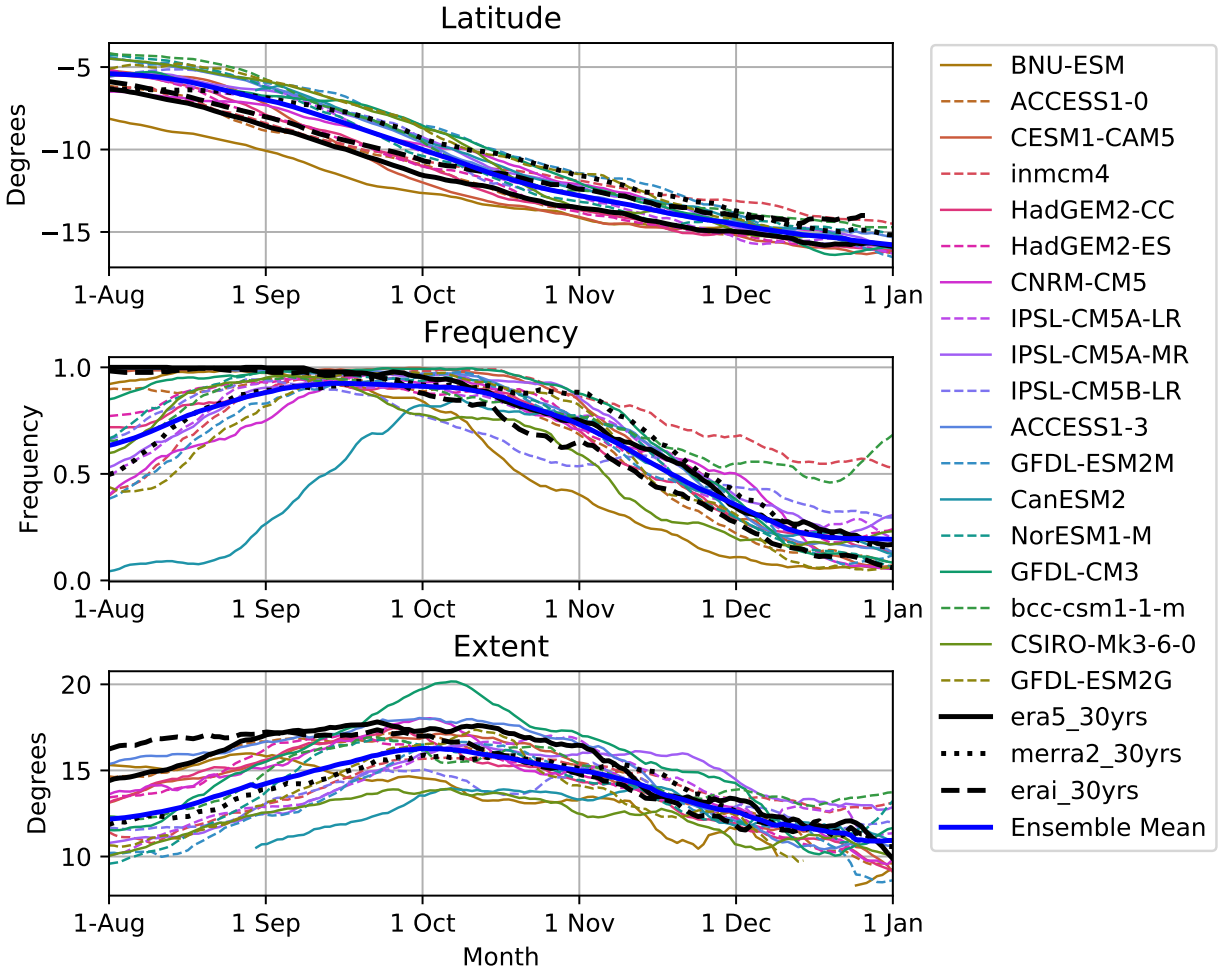

FIG. 5. Seasonal cycles of CAB properties. Top: mean CAB latitude, second row: CAB frequency, and third row: CAB extent (number of grid cells identified per day). Thin colored lines indicate models, and are ordered by the mean CAB latitude averaged from August to November. Black lines show reanalysis products, thick blue lines show the ensemble mean. All quantities are smoothed by a 2-week running mean.

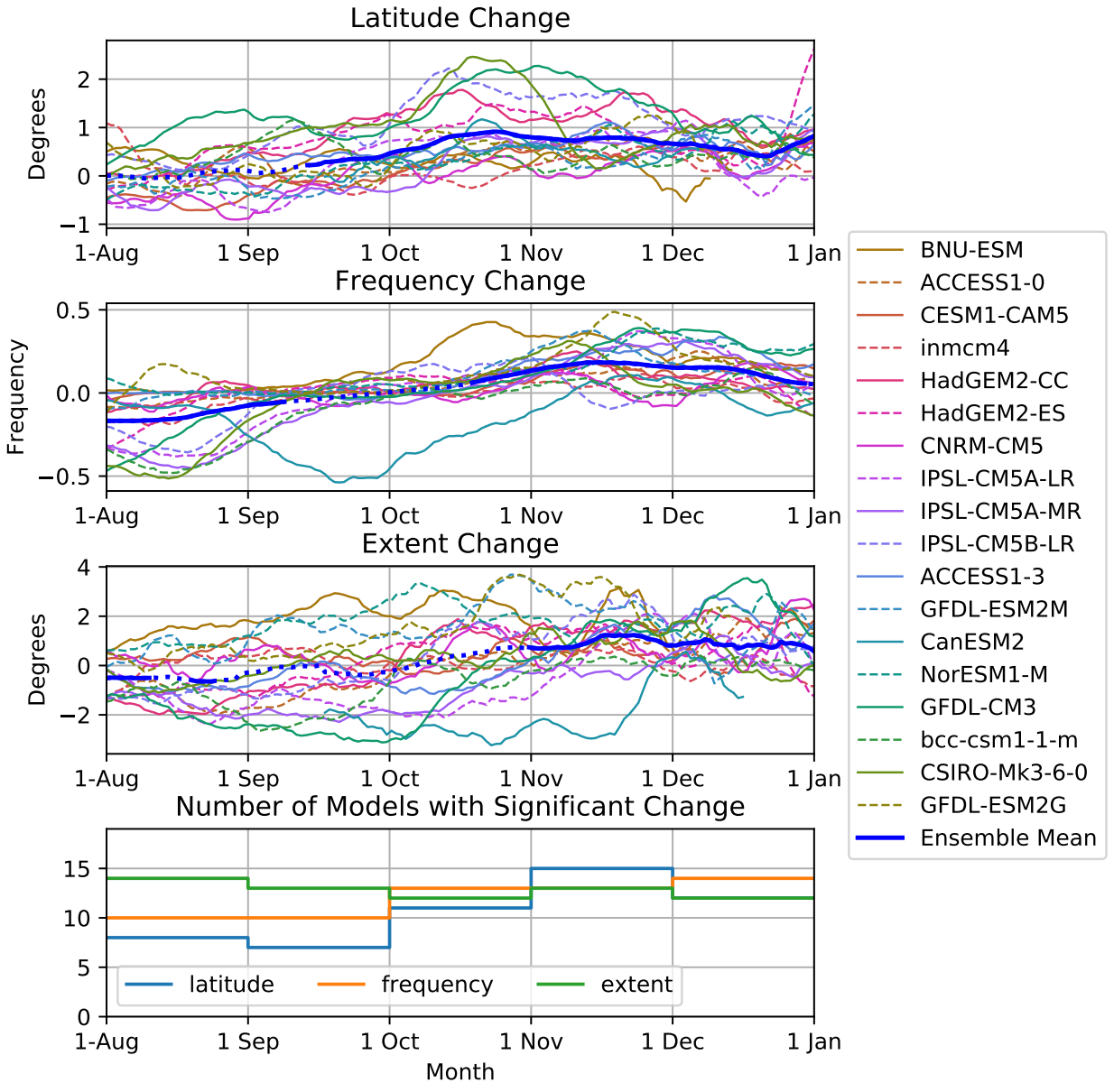

FIG. 6. Seasonal cycles of future change of CAB properties. As per Figure 5, but showing the average of each property for the RCP8.5 end of 21st century scenario, minus that for the historical end of 20th century scenario. The thick blue line indicates the ensemble mean and is shown as a solid line when the ensemble mean is significantly different from zero at the $p < 0.05$ level using a paired t-test, and a dotted line otherwise. All quantities are smoothed by a 2-week running mean. The bottom panel indicates the number of models for which the future change signal is significant against internal variability at a $p < 0.05$ level for each month, using a Welch's t-test. Colors are ordered as per Figure 5. Colors in the top 3 panels are ordered as per Figure 5.

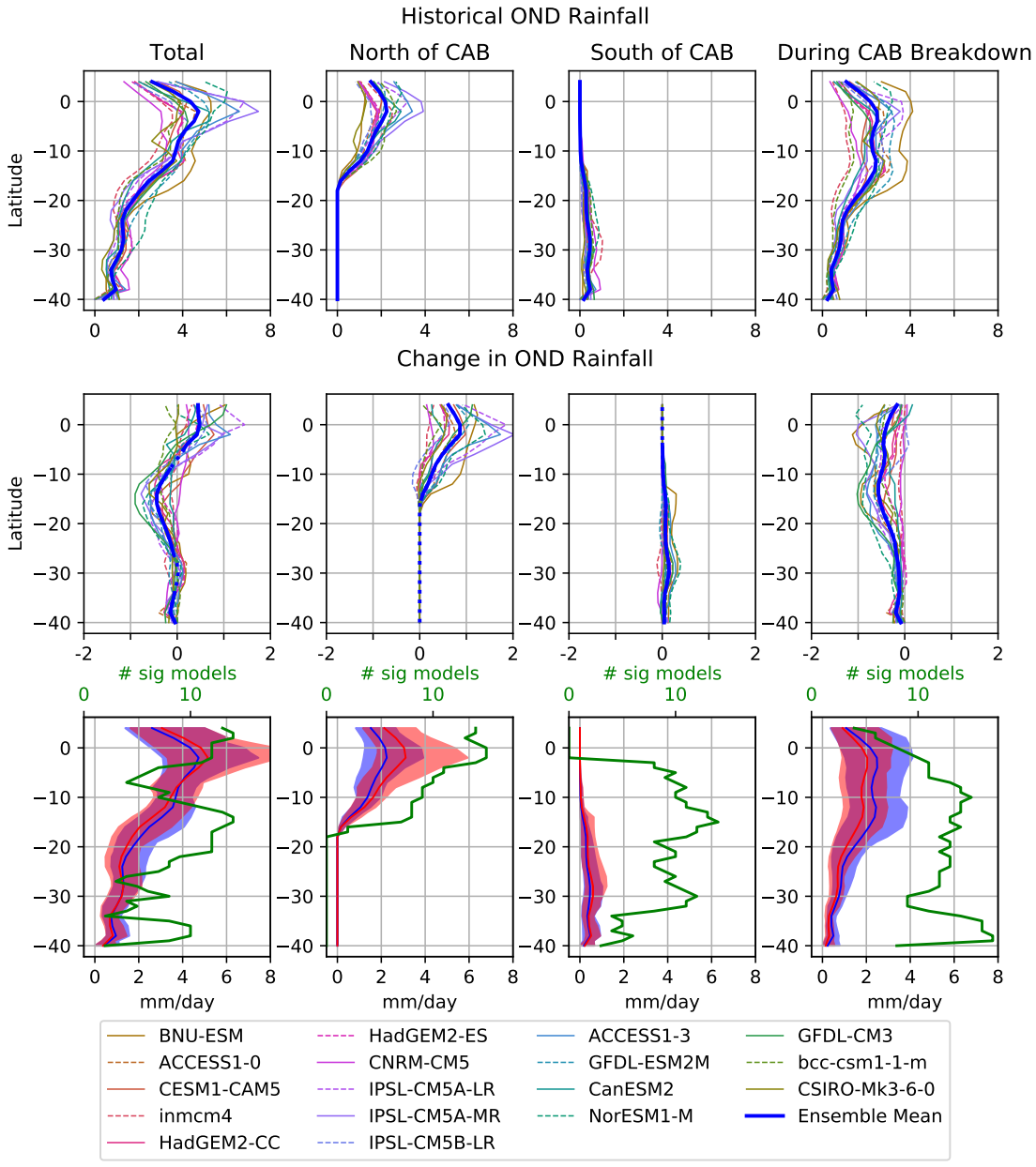

FIG. 7. CAB rainfall decomposition. Top row: historical rainfall, middle row: RCP8.5 minus historical. The bottom row compares the inter-model spread in historical (blue) and RCP8.5 (red) simulations, and shows the number of models which exhibit a significant change relative to interannual variability at the $p < 0.05$ level, based on a paired t-test (green line, top axis labels). First column: total rain. Following columns show rainfall that falls: north of the CAB (second column), south of the CAB (third column) and during CAB break down (last column). All panel show October - December mean. Colors are ordered as per Figure 5.

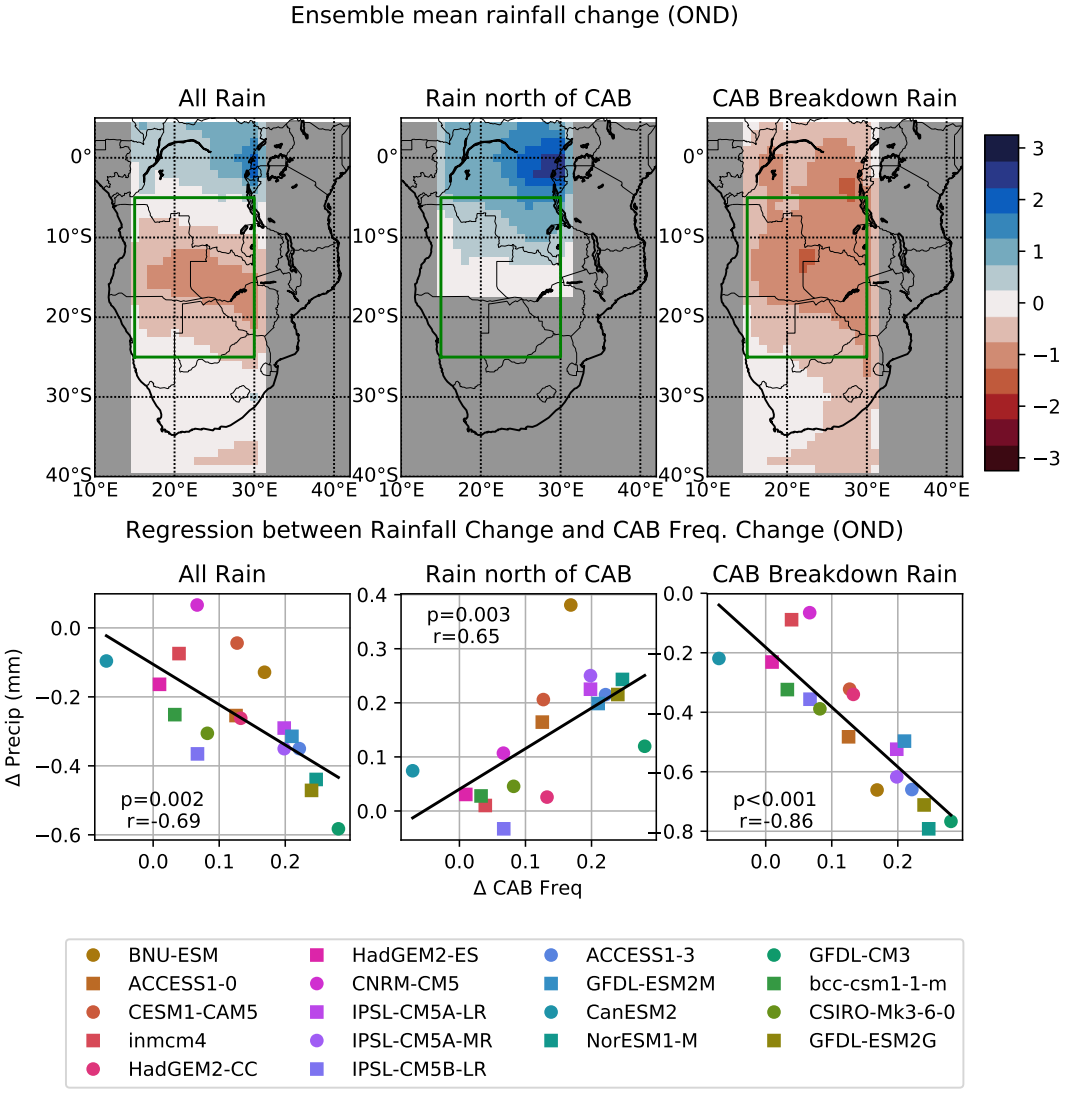

FIG. 8. Top row: Ensemble mean rainfall change OND based on CAB decomposition. Bottom row: Linear regression between rainfall OND change in the region 15°-30 °E, 5°-25°S and the November-December CAB frequency change. Black line: least squares regression, text: p-value for the test that the slope of the regression is equal to zero, and Pearson's correlation coefficient. Left column: total rainfall, centre column: rain that occurs north of the CAB, right column: rain that occurs during CAB breakdown events. Colors are ordered as per Figure 5.

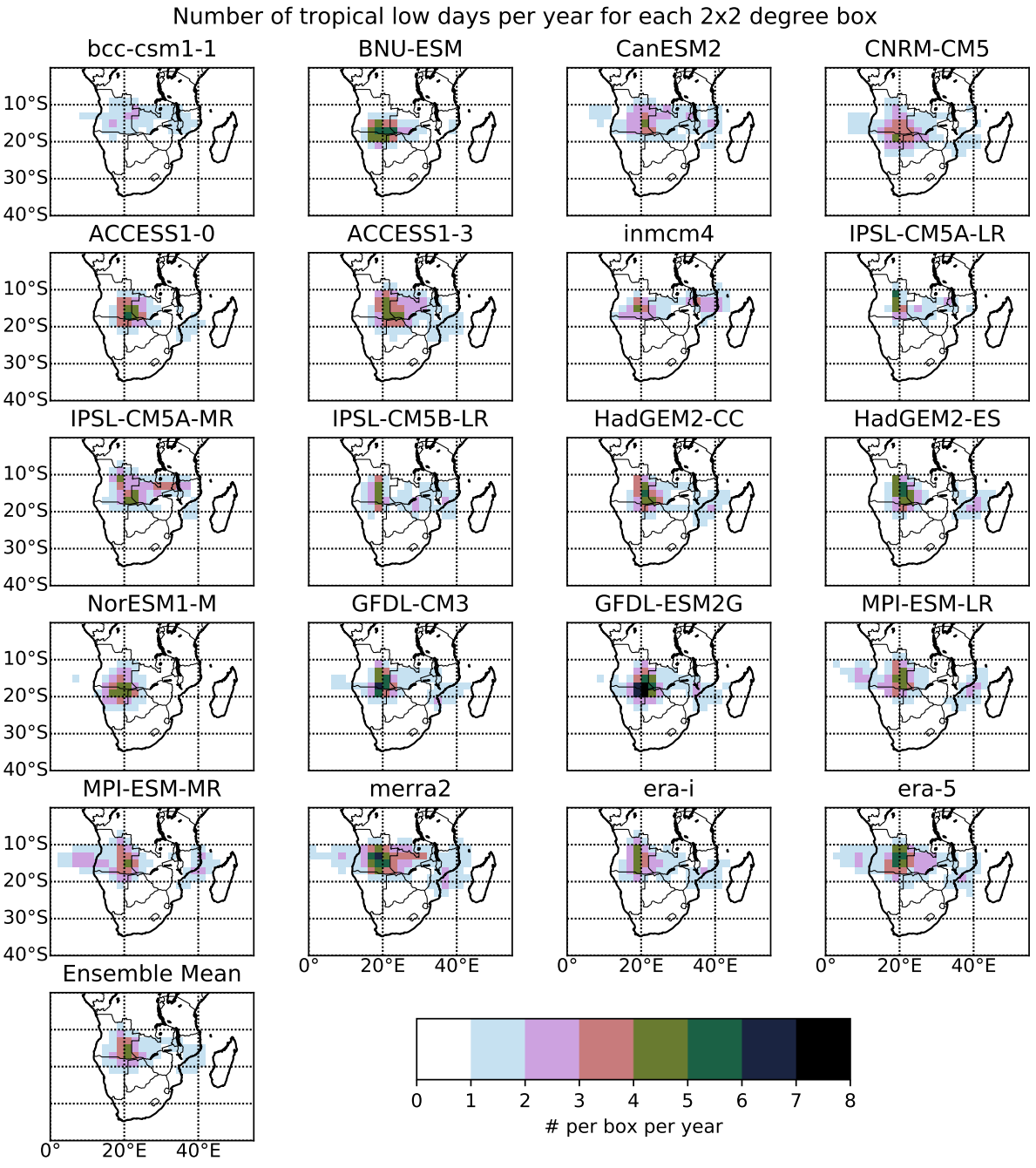

908 FIG. 9. Spatial distributions of tropical lows per 2 × 2° grid cell. Panels indicate different models, ensemble
909 mean and reanalysis products.

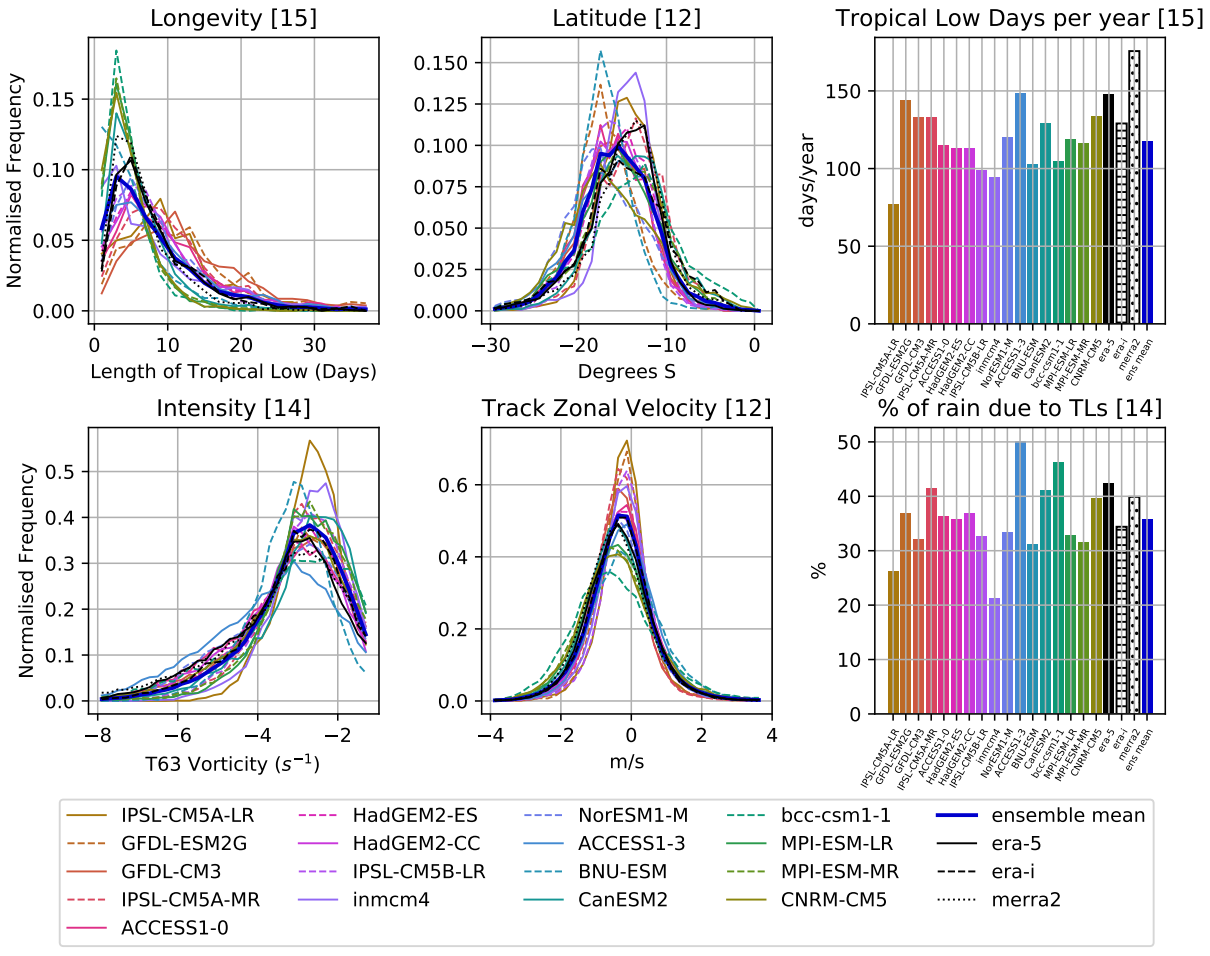

910 FIG. 10. Normalized distributions (left and centre) and overall quantities (right) of tropical low properties.
911 Top left: Longevity of TL events in days. Top centre: track latitude. Top right: total number of tropical low
912 days per year for each model/reanalysis product. Bottom left: T63 filtered vorticity. Bottom centre: track zonal
913 velocity, calculated as the tendency of the track longitude. Bottom right: proportion of rainfall attributable to
914 tropical lows, based on the methodology described in section 4b averaged over 15°-30°E and 10°-25°S. Thin
915 colored lines indicate models, and are ordered by the maximum bin frequency of the upper left panel. Black
916 lines show reanalysis products, thick blue lines show the ensemble mean. Numbers in brackets indicate the
917 number of models which show a significant change relative to natural variability at a $p < 0.05$ level based on a
918 Mann Whitney U-test for the left column, and a Welch's t-test for the remaining panels.

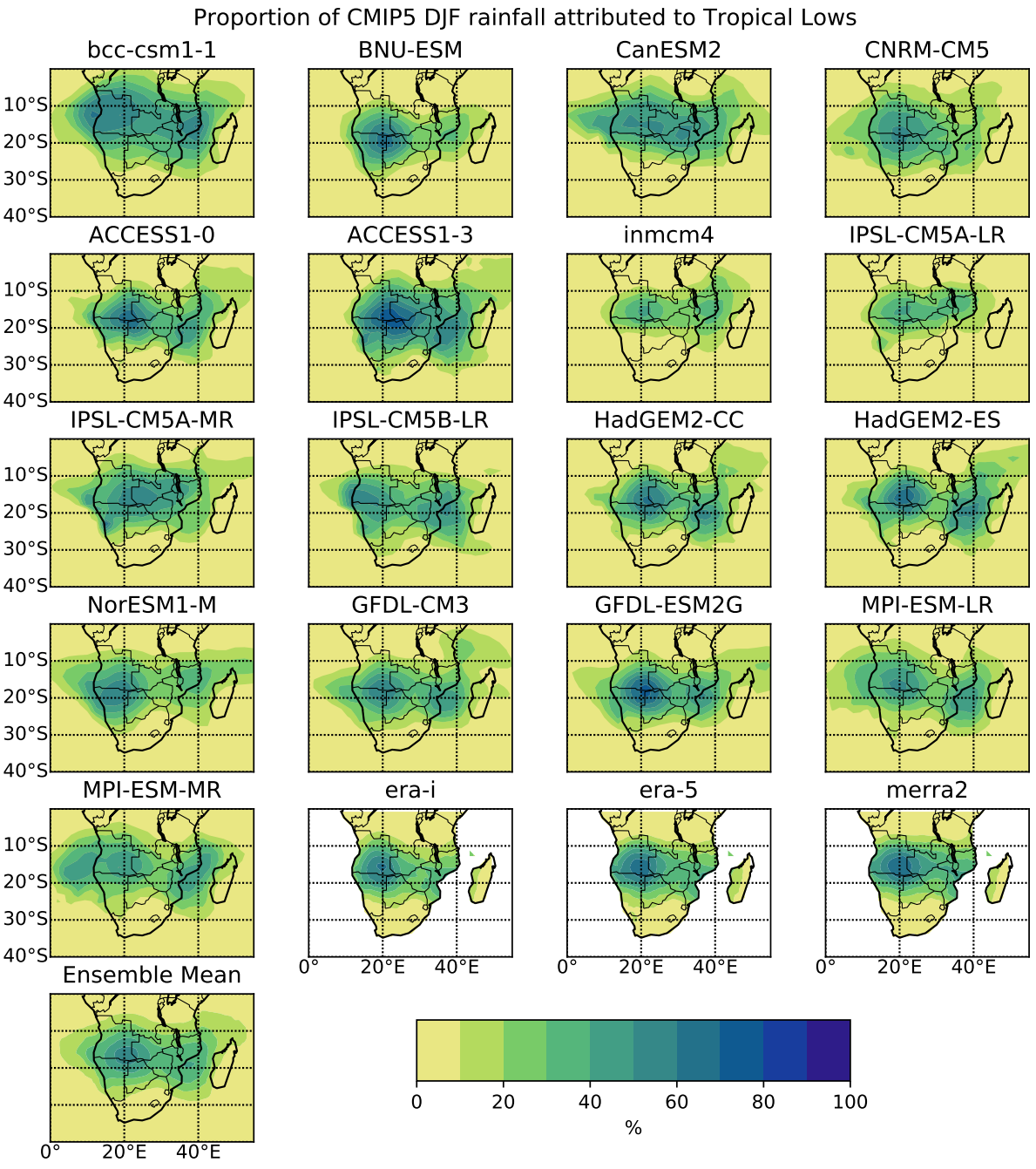

FIG. 11. Proportion of rainfall attributed to tropical lows from December to February in historical CMIP5 sample. Rainfall is defined to be associated to a tropical low if it falls within 5° of the tropical low centroid. Panels show different CMIP5 models and the ensemble mean.

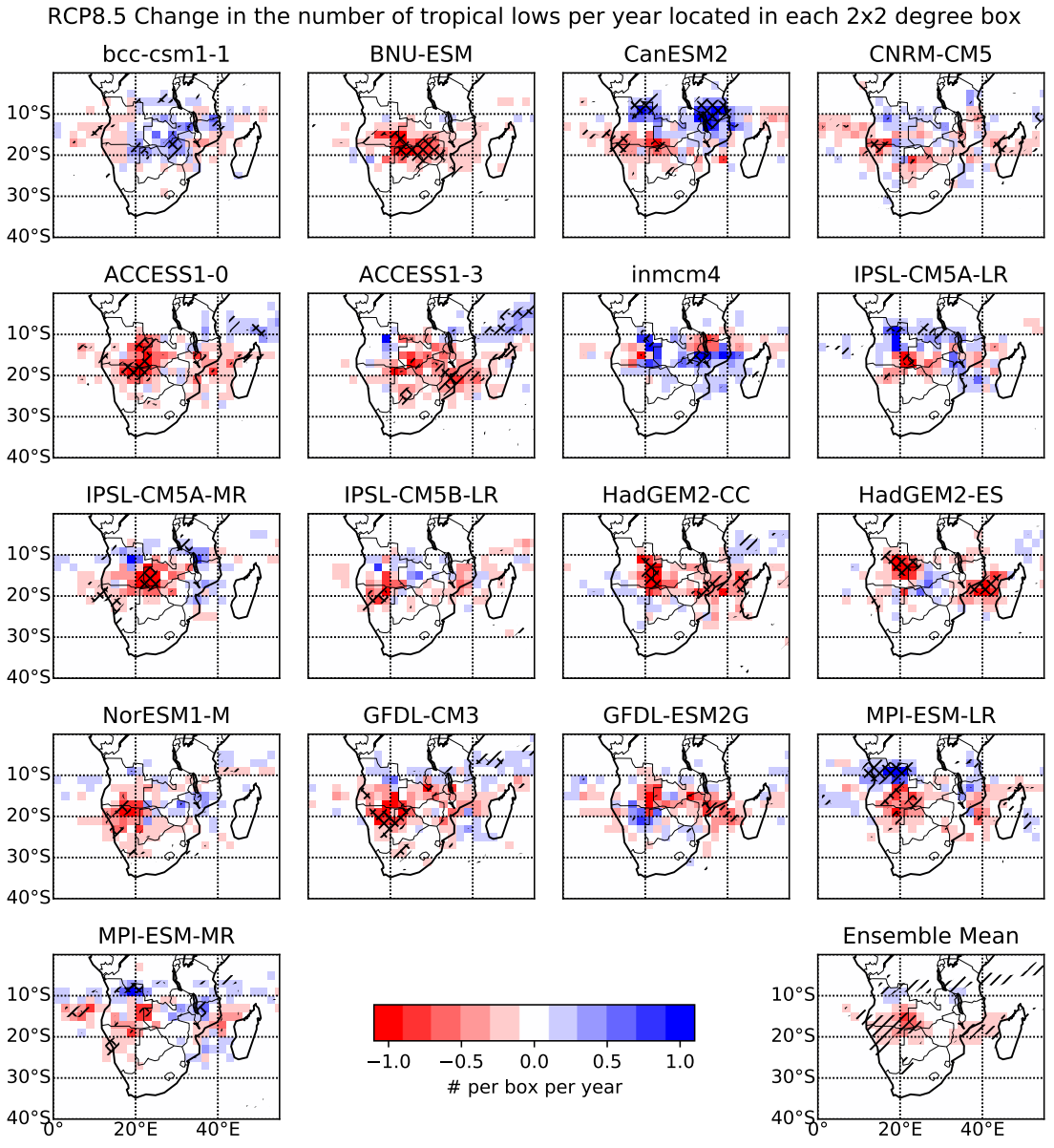

922 FIG. 12. Changes in the distributions of tropical lows per grid-box per year between the RCP8.5 sample and
923 the historical sample in each model and in the ensemble mean. Hatching on individual model panels indicates
924 changes that are significant relative to interannual variability using a Welch's t-test. Forward (backward) hatch-
925 ing indicates significance at a $p < 0.1$ ($p < 0.05$) level. Ensemble mean: forward hatching indicates changes
926 that are significant relative to the inter-model spread at a $p < 0.05$ level using a paired t-test.

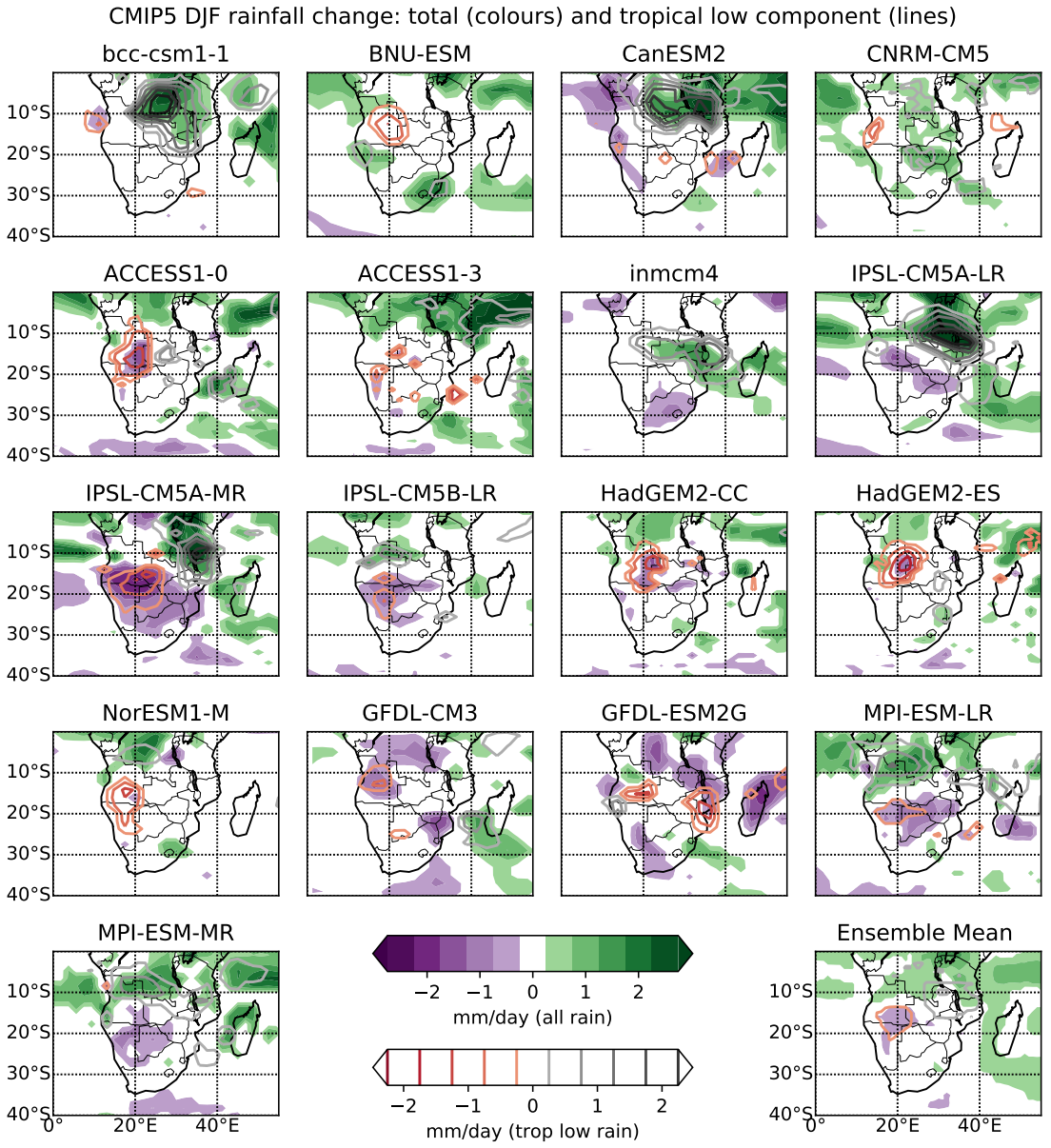

927 FIG. 13. Filled contours: total rainfall change between RCP8.5 end of 21st century sample and historical end
928 of 20th century sample for December to February over southern Africa. Purple: decrease, green: increase. Line
929 contours: same as filled contours, but only for rainfall that has been attributed to tropical lows. Data that is
930 insignificant at a $p < 0.05$ level relative to interannual variability (inter-model spread) based on a Welch's t-test
931 (paired t-test) is masked for each model (for the ensemble mean).

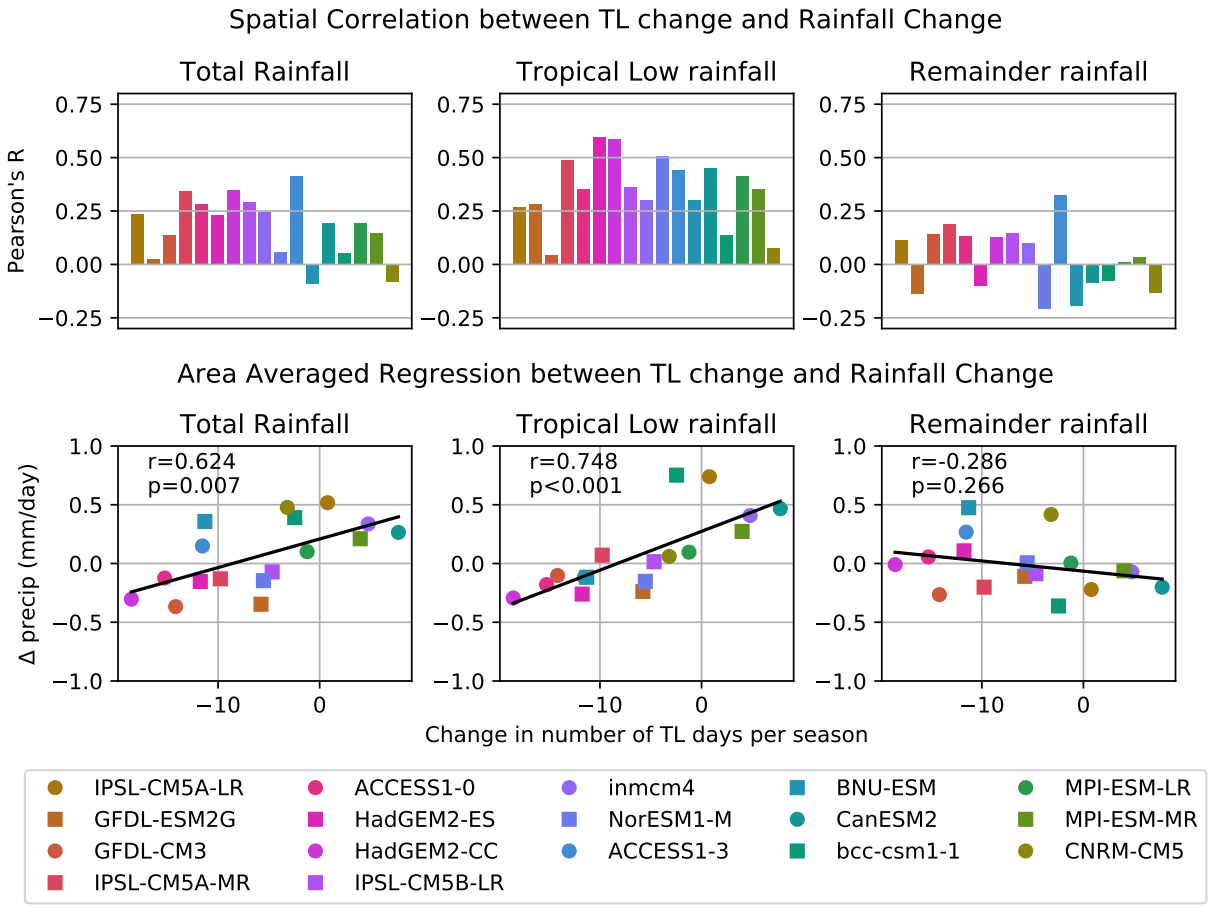

FIG. 14. Upper row: spatial correlation between rainfall change components and tropical low spatial distribution change. Rainfall change and tropical low distribution change were calculated on a 2°×2° grid before correlation, and only mainland points between 5°-25°S were considered. Lower row: inter-model regression between overall rainfall change and tropical low frequency change, averaged over the same region as listed above. Left column: change in total rainfall field. Centre column: change in rainfall located within 5 degrees of a tropical low. Right column: remainder rainfall.